



Review

Monitoring Volcanic Plumes and Clouds Using Remote Sensing: A Systematic Review

Rui Mota , José M. Pacheco , Adriano Pimentel and Artur Gil *

IVAR-Instituto de Investigação em Vulcanologia e Avaliação de Riscos, Universidade dos Açores,
9500-321 Ponta Delgada, Portugal; rui.ms.mota@uac.pt (R.M.)

* Correspondence: artur.jf.gil@uac.pt

Abstract: Volcanic clouds pose significant threats to air traffic, human health, and economic activity, making early detection and monitoring crucial. Accurate determination of eruptive source parameters is crucial for forecasting and implementing preventive measures. This review article aims to identify the most common remote sensing methods for monitoring volcanic clouds. To achieve this, we conducted a systematic literature review of scientific articles indexed in the Web of Science database published between 2010 and 2022, using multiple query strings across all fields. The articles were reviewed based on research topics, remote sensing methods, practical applications, case studies, and outcomes using the Preferred Reporting Items for Systematic Reviews and Meta-Analyses (PRISMA) guidelines. Our study found that satellite-based remote sensing approaches are the most cost-efficient and accessible, allowing for the monitoring of volcanic clouds at various spatial scales. Brightness temperature difference is the most commonly used method for detecting volcanic clouds at a specified temperature threshold. Approaches that apply machine learning techniques help overcome the limitations of traditional methods. Despite the constraints imposed by spatial and temporal resolution and optical limitations of sensors, multiplatform approaches can overcome these limitations and improve accuracy. This study explores various techniques for monitoring volcanic clouds, identifies research gaps, and lays the foundation for future research.

Keywords: remote sensing; volcanic clouds; volcanic plumes; monitoring; systematic literature review



Citation: Mota, R.; Pacheco, J.M.; Pimentel, A.; Gil, A. Monitoring Volcanic Plumes and Clouds Using Remote Sensing: A Systematic Review. *Remote Sens.* **2024**, *16*, 1789. <https://doi.org/10.3390/rs16101789>

Academic Editor: Ciro Del Negro

Received: 15 March 2024

Revised: 7 May 2024

Accepted: 16 May 2024

Published: 18 May 2024



Copyright: © 2024 by the authors. Licensee MDPI, Basel, Switzerland. This article is an open access article distributed under the terms and conditions of the Creative Commons Attribution (CC BY) license (<https://creativecommons.org/licenses/by/4.0/>).

1. Introduction

Explosive volcanic eruptions are hazardous natural events that can have severe consequences at local, regional, and even global scales. They can produce large amounts of volcanic particles (mostly ash) and gases (e.g., H₂O, CO₂, and SO₂) that are carried upward in the atmosphere by convective volcanic plumes or laterally transported by ground-hugging pyroclastic density currents [1]. As volcanic clouds spread into the atmosphere, they become progressively diluted by the air's entrainment and particles' settling. Among many factors, the dispersal of ash depends on the dynamics and height of the volcanic plume, particle characteristics, sedimentation processes, and atmospheric conditions (wind advection, atmospheric turbulence, temperature, etc.) [1,2]. Volcanic ash can be transported over very long distances from the source (up to thousands of kilometers) and remains airborne for extended periods (several months) [3,4]. Thus, volcanic ash can potentially affect large land, ocean, and airspace areas, threatening human health, land and water ecosystems, critical infrastructure, economic sectors, agricultural areas, ground transportation, air traffic, and, in extreme cases, the global climate [5].

It is crucial to accurately detect, monitor, and forecast their dispersion to mitigate the hazardous consequences of volcanic clouds. Several methods are available for achieving this objective, including ground-based techniques [6–8], aircraft/unmanned aerial vehicles (UAVs) [9,10], satellite remote sensing [11–13], and numerical forecasting models [14]. In

addition, multiplatform approaches can improve volcanic cloud detection and provide more reliable forecasting results [15,16].

These methods are used by some volcano observatories and by volcanic ash advisory centers (VAACs), which typically combine remote sensing approaches with volcanic ash transport and dispersion models (VATDMs) [17,18]. However, various factors can limit volcanic cloud forecasting. A forecast's reliability depends on the input data's accuracy, which relies on other models, direct measurements, and remote sensing retrievals. Numerical forecasts are heavily dependent on the estimation of eruptive source parameters (ESPs), particularly the mass eruption rate (MER), total grain size distribution (TGSD), and plume height, which are often difficult to obtain with the necessary accuracy during the first few hours of an eruption. Plume height is of the utmost importance and can be obtained more accurately by volcano observatories using ground-based techniques in the first stages of an eruption, which are then used to trigger operations in VAACs [19].

After the eruptions of Eyjafjallajökull in 2010 and Grímsvötn in 2011, the International Civil Aviation Organization (ICAO) established ash concentration thresholds to mitigate air traffic risks. Zehner [20] translated the specific requirements for improved volcanic ash monitoring and forecasting. These include the early detection of volcanic emissions and near real-time global monitoring of volcanic clouds with open access and data delivery [21], as well as quantitative retrievals of volcanic ash, SO₂ concentrations, and altitudes from satellite instruments and their validation [22].

The purpose of this review article is threefold as the following: (1) to identify the research approaches used to detect and monitor volcanic clouds and estimate ESP using remote sensing data; (2) to characterize the different approaches for identifying and comparing the advantages and shortcomings of retrieval methods; and (3) to identify possible research gaps for future developments and support a research agenda on this topic. To achieve these goals, a systematic literature review was conducted using the Preferred Reporting Items for Systematic Reviews and Meta-Analyses (PRISMA) statement as a guideline [23].

2. Methodology

To identify relevant studies on volcanic plume and cloud detection and monitoring, we conducted a systematic literature review of scientific articles indexed in the Web of Science database using the Preferred Reporting Items for Systematic Reviews and Meta-Analyses (PRISMA) statement as a guideline [23].

The search parameters used were keywords chosen based on the review topic. Keywords were combined as the following: "Volcanic cloud" OR "Volcanic plume" OR "Volcanic column" AND "Ash plume" OR "Ash cloud" OR "Plume" AND "Remote sensing" OR "Satellite" AND "Monitoring" AND "Eruptive source parameters" OR "SO₂ mass flux" OR "SO₂ flux". Only articles published in peer-reviewed journals between 1 January 2010 and 31 December 2022 were considered for this analysis (link for the Web of Science query, last visited on 20 November 2023: <https://www.webofscience.com/wos/woscc/summary/21923291-7faa-4022-923e-86244a6a12c0-b114db3d/relevance/1>). This research focused explicitly on original articles, and thus, review, conference, and proceedings articles were excluded from the search [24,25].

The goal of this work was to examine remote sensing approaches used to detect and monitor volcanic plumes and clouds and estimate eruptive source parameters and the only articles that were selected included the following criteria: (1) ash plume retrievals, SO₂ retrievals, or a combination of both; (2) remote sensing methods and data combined with numerical forecasting of volcanic plumes and clouds; (3) detection and monitoring of volcanic plumes and clouds in near real-time; and (4) estimation of eruptive source parameters.

In total, 828 scientific articles were identified during the initial queries. These articles were all reviewed by analyzing their titles and abstracts. This resulted in the second and finer selection of 360 articles that met the keywords and related research criteria. A total of

238 articles were excluded because they did not meet the inclusion criteria defined above or had a broader scope, resulting in a final selection of 122 articles (Figure 1).

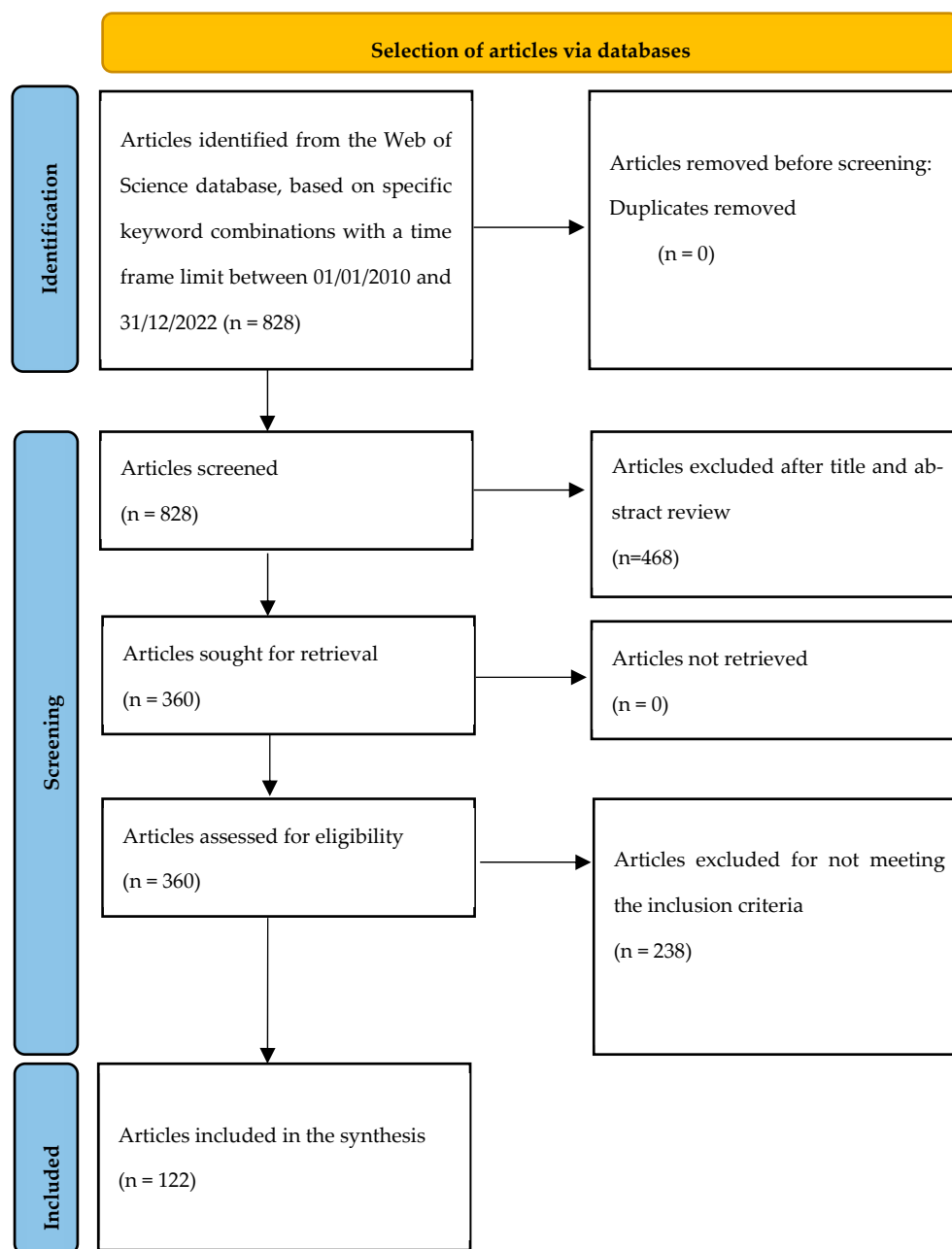


Figure 1. Systematic review procedure for article selection.

The final dataset was categorized based on five identified methodological approaches for volcanic cloud detection and monitoring. It was divided into five research categories: (A) satellite-based remote sensing for volcanic cloud detection and monitoring; (B) ground-based remote sensing for volcanic plume and cloud monitoring; (C) airborne/UAV-based remote sensing for volcanic cloud monitoring; (D) multiplatform approaches for volcanic plume and cloud monitoring; and (E) remote sensing data assimilation to numerical forecasting models.

3. Results

Analysis of the final selection of scientific articles revealed the vast scope of this topic in the scientific literature, with articles published in 41 peer-reviewed scientific journals (Figure 2). Most of these journals have diverse subjects and scopes, such as remote sensing, climate, robotics, geosciences, and atmosphere. The top six journals account for 60% of the articles analyzed, with the remaining 40% distributed across 35 other journals.

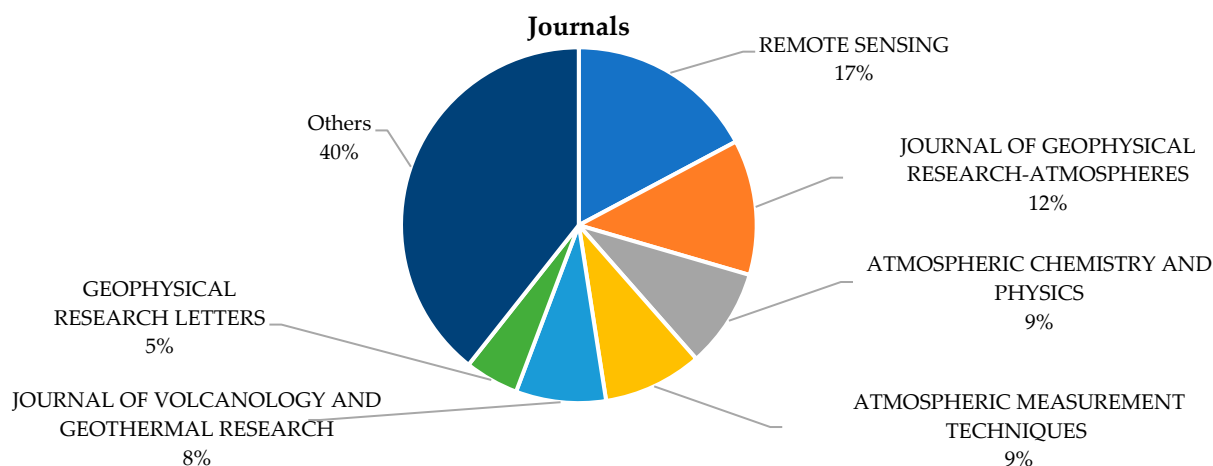


Figure 2. Distribution of peer-reviewed scientific journals (top 6 highlighted).

Based on the case studies (Figure 3), we observed a wide range of volcanoes covered in 122 articles (43 volcanoes in total). The Eyjafjallajökull 2010 eruption alone was represented 26 times, making it one of the best-studied eruptions. The eruptions of the Etna volcano accounted for 34 of the total case studies, as it was also one of the best-monitored volcanoes in the world. The top five studied volcanoes appeared 81 times as case studies in the selected articles.

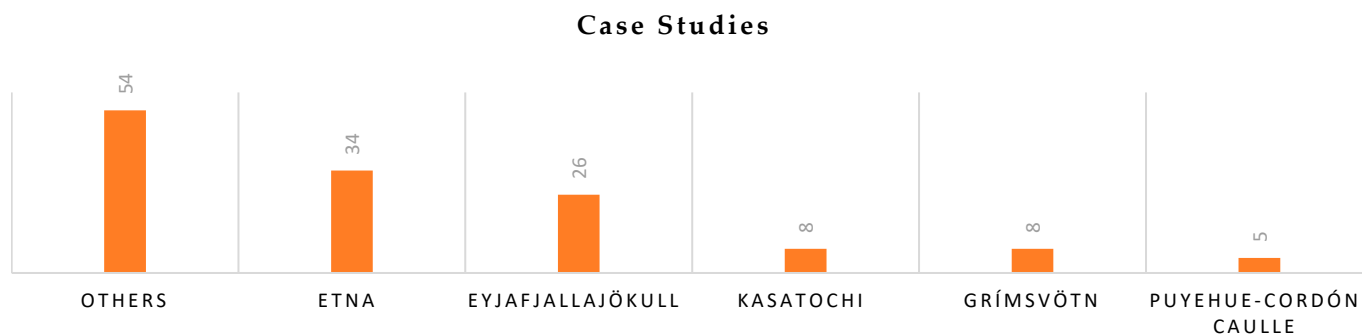


Figure 3. Distribution of case studies (top 5 highlighted).

Regarding the research categories, 46% of the selected scientific articles were related to “A-Satellite-based remote sensing for volcanic cloud monitoring” (Figure 4).

All the information collected and processed for this review article is provided in the Supplementary Materials.

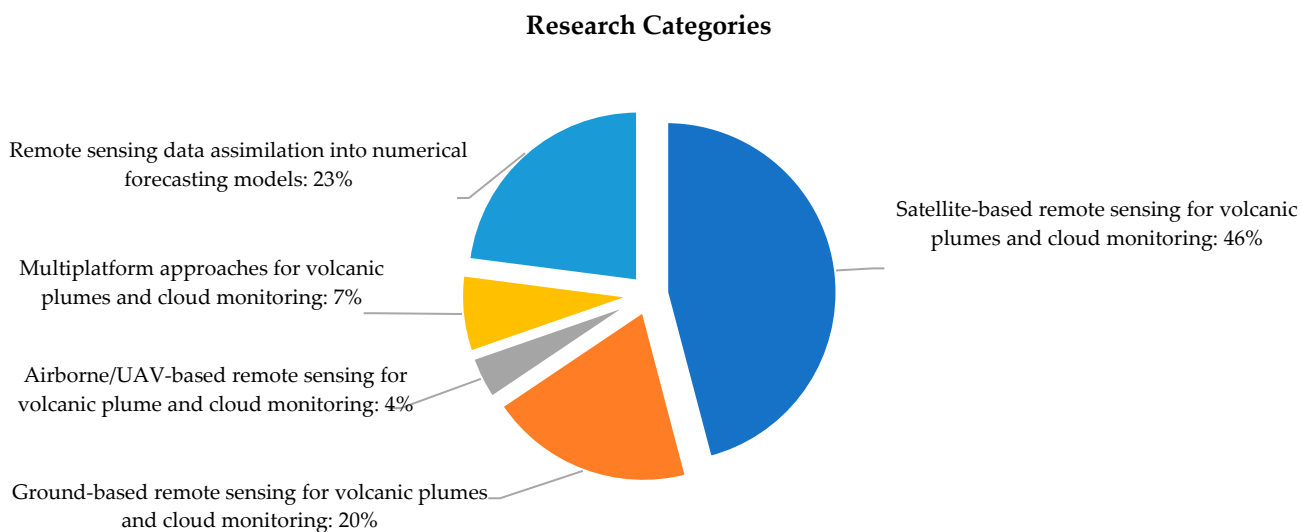


Figure 4. Distribution of research categories.

4. Discussion

4.1. A-Satellite-Based Remote Sensing for Volcanic Plumes and Cloud Monitoring ($n = 56$)

Table 1 summarizes the articles obtained from the systematic review procedure, which focused on satellite remote sensing-based approaches for monitoring volcanic clouds. Their main objectives were ash and SO_2 retrieval from volcanic eruptions using satellite sensors and applying specific algorithms and techniques. These data are critical for tracking and managing volcanic hazards, allowing for rapid responses and ensuring the safety of people and infrastructures in volcanic areas.

Satellite data-driven approaches are the most used method for monitoring volcanic clouds and able to monitor at a global scale and in near real-time, primarily because of the wide coverage and the increasing availability of open-access data, being cost-effective [26,27] and particularly relevant for studying remote volcanoes. Earth observation (EO) sensors have recently become standard tools for operational agencies to track the movement of volcanic clouds and measure key parameters (e.g., ash mass, SO_2 mass, and plume height) to provide alert information [28–30]. Many EO satellites carry sensors that are capable of detecting and measuring volcanic clouds. The abundance of sensors and data has led to a new era in research. Instruments such as the Spinning Enhanced Visible and Infrared Imager (SEVIRI) and Advanced Himawari Imager (AHI) have very high temporal resolutions of 15 and 10 min, respectively, using infrared (IR) technology [31,32], allowing for day and night monitoring. For ash retrieval, techniques such as brightness temperature difference (BTD) algorithms use spectral differences between volcanic clouds and the background environment [29,33] to quantify ash parameters. Ultraviolet (UV) sensors onboard satellites, such as ozone monitoring instruments (OMIs) and tropospheric monitoring instruments (TROPOMIs), have been used to assess volcanic SO_2 emissions [13,34,35].

Based on this analysis, we conclude that satellite remote sensing data approaches are the most commonly used techniques for volcanic plume and cloud detection and monitoring and quantification of ESP and that the sensors used for volcanic ash and SO_2 monitoring span the electromagnetic spectrum from UV to microwave radiation. In the IR region, spectral bands at wavelengths of 11 and 12 μm are normally used for the detection of ash, while 7.3 and 8.7 μm are used for SO_2 detection. In the UV region, spectral bands between 280 and 340 nm were used for measurements of SO_2 .

Table 1. Summary of articles related to satellite-based remote sensing for volcanic cloud monitoring ($n = 56$).

Reference	Case Study	Data Source	Retrieval Method	Main Outcomes
[11]	Kasatochi 2008	MODIS, AVHRR, and AIRS	BTD, LUT, and least square fit method	Plume height ≈ 17 km. Total mass ash $\approx 0.46 \pm 0.18$ Tg. Total mass SO ₂ $\approx 2.65 \pm 0.82$ Tg. SO ₂ mass < 30–40% of the uncorrected values.
[31]	Etna 2002	MODIS and SEVIRI	RSTash	Space–time detection of the evolution of ash clouds.
[12]	Kasatochi 2008	IASI	BTD, RTM, and OE method	Plume height $\approx 12.5 \pm 4$ km. Total SO ₂ ejected mass ≈ 1.7 Tg.
[36]	Etna 2002, 2006/7	AVHRR	BTD-Water Vapour C correction and RSTash	The capability of RSTash to account for water vapor content in the atmosphere without requiring any ancillary information.
[37]	Etna 2006/7	MODIS, AVHRR, and SEVIRI	RSTash BT	The success and failure rates of RSTas identifying ash are 90.1% and 9.9%.
[38]	Eyjafjallajökull 2010	SEVIRI, AIRS, GOME2, IASI, and OMI	OE method and RTM	Plume height ≈ 6 km. Total mass ash ≈ 1.05 Tg. Total mass SO ₂ ≈ 0.013 – 0.073 Tg. Plume altitude error = 20% or 15%. Ash mass loadings = 50%. SO ₂ loadings error = 400 DU.
[39]	Eyjafjallajökull 2010	MODIS, MERSI, and VIRR	SWTD (BTD) and STVA	STVA is more sensitive to volcanic ash clouds than SWTD and provides comparable results to ARI and AAI. FY-3A-derived STVA is effective under complex meteorological conditions.
[40]	Etna 2000/01/02/03/06 & 08	MISR	MINX V1.0 Software	Plume height ≈ 9.2 km. AOD = 0.03 ad 0.58. MINX tool uncertainties < 0.5 km.
[41]	Eyjafjallajökull 2010	MISR	Research Aerosol Retrieval Algorithm and MISR V22 Standard algorithm	Plume height ≈ 9.5 km. Non-spherical grains = 60% of the AOD. Uncertainties using $\chi^2 = 5\%$ of the observed reflectance.
[42]	Eyjafjallajökull 2010	SEVIRI and MODIS	BTD	$R^2 = 0.73$ for AOT retrievals.
[21]	Eyjafjallajökull 2010	SEVIRI	BTD and RTM	Plume height ≈ 6 km. Ash concentration = 5 mg/m^{-3} . 4.8 Mt of ash and 0.2 Mt of SO ₂ were released.
[43]	Grímsvötn 2011 & Eyjafjallajökull 2010	GOME-2, OMI, and SCIAMACHY	Linear Fit (LF) algorithm and DOAS	About 50–80% of the observations were correctly forecast (hits).
[44]	Eyjafjallajökull 2010	MODIS and SEVIRI	CO ₂ Absorption method and BTD	Plume height ≈ 12 km (Starting). Plume height 3–4 km (Ending). Error = 0.6 km. With sub-pixel image matching, the estimates of shifts could be enhanced to about 10–20% of the pixel size.

Table 1. Cont.

Reference	Case Study	Data Source	Retrieval Method	Main Outcomes
[45]	Redoubt 2009	MODIS, MISR, and AVHRR	BTD and MINX V1.0 Software	Plume height from 10.2 km (03/23/2009) to ≈ 20 km (event 8). Positive correlation between plume temperature height retrieval and optical depth. MISR can determine the heights of plumes when the satellite temperature method will produce very poor results.
[26]	Eyjafjallajökull 2010	MODIS	Diffusion source detection algorithm combining SWTD with SO_2	The approach proposed by integrating the split window algorithm with the SO_2 concentration distribution achieves an excellent detection effect of the volcanic ash cloud diffusion source and has a high consistency with volcanic ARI and AAI.
[46]	Shinmoedake 2011	MTSAT-1R and MTSAT-2 Imager	RSTash and BT	Plume height ≈ 7.5 km. Mass eruptive rate $\approx 9.4 \times 10^5$ kg/s (phase I) to 5.4×10^5 kg/s (phase III). Validation analysis success rates = 90.1%.
[30]	Eyjafjallajökull 2010	MODIS	PCA	Band 36 has the largest contribution to the volcanic ash cloud with 72%, followed by bands 31 (67%) and 30 (65%). Bands 36, 31, and 30 are used to eventually detect volcanic ash after the sensitivity analysis.
[47]	Eyjafjallajökull 2010	SEVIRI	NN, LUT, and VPR	Plume height ≈ 8 km. SO_2 total mass maximum differences for all procedures = $+/- 15\%$ and $+/- 10$.
[48]	Grímsvötn 2011	SEVIRI and IASI	(1D-Var) retrieval algorithm for ash and BTD method	SO_2 remained for 2 weeks. Ash was composition was 50–52% SiO_2 .
[49]	Eyjafjallajökull 2010 & Grímsvötn 2011	GOME-2 and IASI	ULB and Oxford Algorithms	R^2 for SO_2 mean loading Oxford and UBL = 0.85/ SO_2 loading estimated by IASI and GOME-2 = 0.64.
[50]	Eyjafjallajökull 2010	SEVIRI	BTD and RTM	Uncertainty due to particle shape increases the error in the total mass of the ash cloud from about 40% to about 50%.
[51]	Eyjafjallajökull 2010	MODIS	PCA	PCA method has good effect in the detection of volcanic ash clouds, whose spectral matching rate of volcanic ash reaches 74.65 and 76.35% and has high consistency with AAI distribution.
[52]	Etna 2011	SEVIRI	VPR and LUT	Ash total mass = 1200 to 3000 tons/h. SO_2 total mass = 1600 to 3500 tons/h. The results show good agreement between methods.
[53]	Kelud 2014	AVHRR and IASI	BTD and RTM	Ash plume top ≈ 18 km. Underlying ice clouds reduce the ash needed to reproduce the measured IASI spectra by about a factor of 12.

Table 1. Cont.

Reference	Case Study	Data Source	Retrieval Method	Main Outcomes
[54]	Etna 2013	MVIRI and SEVIRI	Ash cloud top height (ACTH) based on the apparent shift to Parallax	Plume top height of ≈ 8.5 km. ACTH accuracy is 700 m.
[55]	Eyjafjallajökull 2010	MODIS	VPR and LUT	Total ash and SO ₂ masses differ by about 3 and 10%. Result accuracy reduces to about 50% when the SO ₂ is mixed with ice crystals.
[56]	Puyehue Cordón Caulle 2013	MODIS	BTD	The MODIS-based altitude of the cloud ≈ 3.9 km (a.s.l.). Reverse absorption (BTD-based) ≈ 4.2 km (a.s.l.). MODIS cloud mask detected about 50% of the 16 March 2015 cloud.
[32]	Gunung Agung 2017	AHI	RSTash	RSTASH performance coupled to high temporal resolution of Himawari-8 data may lead to an effective identification and tracking of ash clouds over East Asia and the Western Pacific region despite some limitations.
[57]	Eyjafjallajökull 2010 & Puyehue Cordón Caulle 2011	SEVIRI, AGRI, and CALIOP	FY-4 algorithm using RTM, LSRM, and SWTD (ash detection)	Y-4 algorithm showed reasonable agreement with independent data for plume height. Bias = 0.037 km. Standard deviation = 2.80 km. R ² = 0.61.
[58]	Nabro 2011 & Puyehue Cordón Caulle 2011	OMI, CALIOP, MODIS, AIRS, and GNSS	RO technique	Plume height agreement with RO and CALIOP: R ² = 0.94. Root mean square (r.m.s.) error = 930 m.
[59]	Eyjafjallajökull 2010 & Kasatochi 2008	GOME-2	Full Physics Inverse Learning Machine (FP_ILM)	Kasatochi SO ₂ plume at an altitude in the range 9–10 reaching 14 km (a.s.l.). Eyjafjallajökull plume heights are in the range 6–9 km (a.s.l.). Plume height retrieved with errors of 1 km for high SO ₂ total columns (>50 DU) and a plume height between 6 and 18 km.
[60]	Bogoslof 2017, Tinakula 2017 & Sierra Negra 2018	EPIC	EPIC SO ₂ algorithm	Tinakula SO ₂ loadings 14 kt (21 October).
[61]	Calbuco 2015	MODIS and VIIRS	BTD and parametric retrieval algorithm combined with BTD mask	Plume height = 21 km (a.s.l.). Ash mass of 3.65×10^9 kg. Mass loadings: VIIRS = 0.4 g/m ² ; MODIS = 1.4 g/m ² ; Fine ash $\approx 1\%$ of total ash mass.
[62]	Etna 2013	OLI, MODIS, and SEVIRI	“Dark pixel” procedure and PEM	Landsat cloud height varies from about 6 up to 9.5 km (a.s.l.). MODIS cloud height is 8.9 km (a.s.l.) with an uncertainty of ± 500 m. SEVIRI clout top height is 10.5 km (a.s.l.) with an uncertainty of ± 500 m.

Table 1. Cont.

Reference	Case Study	Data Source	Retrieval Method	Main Outcomes
[34]	Raikoke 2019	TROPOMI	FP_ILM	SO ₂ plume height \approx 13 km (a.s.l.). SO ₂ layer height with an accuracy better than 2 km for SO ₂ total column densities > 20 DU.
[63]	Holuhraun 2014	IASI	OE method, Forward model, and DOAS technique	SO ₂ masses showed a maximum of 0.25 Tg.
[64]	Etna 2018	MODIS	LSTM-CA	Total accuracy of volcanic ash cloud identification reached 96.1%.
[65]	Bogoslof 2016-17	ABI, AVHRR, MODIS, and VIIRS	BTD	The 10 largest events each had a total erupted mass > 1×10^9 k. Total mass for 28 events was 5.7×10^{10} kg. Maximum mass eruption rate 1×10^5 to 4×10^6 kg/s ⁻¹ . 18 of the volcanic clouds reached > 8.5 km (a.s.l) with uncertainty of 10%.
[66]	Etna 2013	OLI	Height-From-Shadow technique and Plume Elevation Model (PEM)	For cloud 1, 84 height measurements were made over the 7.7 km of its downwind extent. There was a gap of 22 km where no cloud was apparent. For cloud 2, for which there were 62 height measurements, extended 19.5 km to the image.
[22]	Etna 2018	SEVIRI	MS2RWS (MeteoSat to Rapid Response Web Service) algorithm, AVHotRR routine	Volcanic plume height \approx 8 km (a.s.l). Ash total mass \approx 35 kt. SO ₂ total mass \approx 100 kt. SO ₂ flux peaks \approx 600/kg/s and mean of \approx 185 kg/s.
[35]	Sinabung 2018	TROPOMI, AHI, SEVIRI, and CALIOP	VADGUS, FRESCO, O22CLD, and ROCINN algorithms	ROCINN height is very similar to the FRESCO $R^2 = 0.98$ from 0.5 and 14 km. The O22CLD and ROCINN are corresponding. FRESCO heights exceeded 15 km (a.s.l).
[67]	Eyjafjallajökull 2010 & Puyehue-Cordón Caulle 2011	SEVIRI and CALIOP	SDA, GA, LSSVR 1D-VAR, and BTD	ACTH combination between methods vs. CALIOP VTH Eyjafjallajökull 2010: SDA-GA-LSSVR $R^2 = 0.77$; GA-LSSVR $R^2 = 0.74$; LSSVR $R^2 = 0.67$; 1D-VAR algorithm $R^2 = 0.38$. Puyehue-Cordón Caulle 2011: SDA-GA-LSSVR $R^2 = 0.79$; GA-LSSVR $R^2 = 0.68$; LSSVR $R^2 = 0.60$; 1D-VAR algorithm $R^2 = 0.27$.
[68]	Etna 2018	MODIS	FF-CNN-LSTM method	Classification accuracy 88.4%. Kappa coefficient = 0.8011
[69]	Etna 2018	SEVIRI, MODIS, VIIRS, TROPOMI, AIRS, and IASI	“Traverse” approach	Plume height \approx 8 km (a.s.l.) Total SO ₂ flux uncertainty estimated to be about 45% (using SEVIRI). TROPOMI and IASI show more sensitivity.

Table 1. Cont.

Reference	Case Study	Data Source	Retrieval Method	Main Outcomes
[70]	Eyjafjallajökull 2010	SEVIRI	BTD, LUT, and RTM based on DISORT	Mass concentration and optical depth at the wavelength of 0.355 μm . $R^2 = 0.79$ and 0.73 , respectively; root mean square error (RMSE) = 0.17 and 0.18 ; mean absolute error (MAE) = 0.11 and 0.14 .
[71]	Etna 2012	IASI	AEROIASI algorithm and RTM- TOVS	SO_2 peaks at 9.5 km and 11.5 km. Total uncertainty for column mass concentration estimations 35% .
[72]	2008 Kasatochi, 2014 Kelud, 2015 Calbuco & 2019 Raikoke	OMI	FP_IML	Plume height error $1\text{--}2$ km.
[73]	Raikoke 2019	TROPOMI, OMPS Limb profiler (LP)	DOAS and PCA	Plume height from 19 to 26 km (a.s.l). Error ≈ 200 m. Peak of stratospheric AOD recorded at a wavelength of 674 nm.
[74]	Raikoke 2019, Taal 2020, Nishinoshima 2020 & La Soufrière 2021	TROPOMI, IASI, and CALIOP	FP_ILM and IASI ULB/LATMOS	SP5 LH, IASI/LATMOS, and mean difference results, respectively: Raikoke, 2019 = 10.18 ± 2.79 km/ 10.03 ± 0.99 km/ -0.15 ± 2.83 km; Taal 2020 = 12.13 ± 3.95 km/ 9.51 ± 1.78 km/ -2.62 ± 3.0 km; Nishinoshima 2020 = 0.73 ± 1.97 km/ 8.0 ± 1.04 km/ 0.27 ± 2.79 km; La Soufrière 2021 = 14.94 ± 3.87 km/ 15.7 ± 1.16 km/ 0.76 ± 3.69 km; S5P SO_2 LH and the CALIOP with bias at -2.5 ± 2 km.
[13]	Raikoke 2019, Sierra Negra 2018, Ulawun 2019 & Etna 2021	TROPOMI	Iterative Covariance-Based Retrieval Algorithm (COBRA)	SO_2 LH error by a factor of 2 to 3 compared to the DOAS algorithm. SO_2 LH accuracy is $1\text{--}2$ km for SO_2 as low as 5DU .
[75]	Hunga Tonga-Hunga Ha'apai 2022	ABI, AHI COSMIC-2, and Spire	Photogrammetry, Automated Stereo-Winds Method, and GNSS-RO technique	Plume height top at $50\text{--}55$ km (a.s.l). GNSS-RO shows most of the plume at $30\text{--}40$ km (a.s.l).
[28]	Eyjafjallajökull 2010	SEVIRI	VADUGS retrieval algorithm	Correlation (0.49), MAPE (90%), MPE ($+55\%$), and RMSE (0.41 g m^{-2}) show that VADGUS can distinguish between thinner and thicker ash pixels although cloud top height is usually strongly underestimated.
[76]	Eyjafjallajökull (2010) and Puyehue-Cordón Caulle (2011)	SEVIRI	VACOS algorithm	Probability of detection (POD) of more than 90% and a false alarm rate (FAR) of ca. 1% . Mean absolute error $\approx 40\%$ or less for ash layers with an OT at $10.8 \mu\text{m}$ of 0.1 or more. ACTH error $\approx 10\%$ for ash above 5 km. Effective radius error of 35% for radii of $0.6\text{--}6 \mu\text{m}$.

Table 1. Cont.

Reference	Case Study	Data Source	Retrieval Method	Main Outcomes
[77]	Raikoke 2019	Sentinel-3 SLSTR and MODIS	NN algorithm and BT	Volcanic cloud detection accuracy of 93% to 99%.
[78]	Tonga-Hunga Há'apai 2022	OMPS-LP	Multi-wavelength aerosol extinction algorithm (OMPS LP operational algorithm)	Top height registered was 50 km (a.s.l.).
[79]	Etna 2020 & 2022	SEVIRI	Machine learning SVM and combination of TIR bands	Ash detection accuracy of 86%.

The detection and quantification of ash and SO₂ have been performed using several multispectral instruments, such as the moderate resolution imaging spectroradiometer (MODIS) [11,26,30,31,37,39,42,44,45,51,55,56,58,61,62,64,65,68,69,77], SEVIRI [21,22,28,31,37,38,42,44,47,48,50,52,54,57,62,67,69,70,76,79], multifunction transport satellite (MTSAT)-1R and MTSAT-2 imagers [46], AHI [32,35,75], advanced baseline imager (ABI) [65,75], and multi-angle imaging spectroradiometer (MISR) [36,37,40]. Hyperspectral instruments, such as the infrared atmospheric sounding interferometer (IASI) [12,38,48,49,53,63,69,71,74] and atmospheric infrared sounder (AIRS) [11,38,58,69], have also been used. Other instruments, such as the advanced very high-resolution radiometer (AVHRR) [11,36,37,45,53,65], visible infrared radiometer (VIRR) [39], operational land imager (OLI) [62,66], visible/infrared imager radiometer suite (VIIRS) [61,65,69], and sea and land surface temperature radiometer (SLSTR) [77] have been used for ash retrieval. SO₂ retrieval in the UV region is commonly performed using hyperspectral sounders, such as OMI [38,43,60,72], scanning imaging absorption for atmospheric cartography (SCIAMACHY) [43], global ozone monitoring experiment-2 (GOME-2) [38,43,49], TROPOMI [13,34,69,74], and ozone mapping and profiler suite (OMPS-LP) [73,78]. Vertical profilers, such as cloud aerosol lidar with orthogonal polarization (CALIOP) [35,57,58,67,74], which is an active sensor in the microwave spectrum (radar) capable of providing vertical profiles of volcanic clouds, allow for more accurate plume height estimations when data are available.

The most commonly applied method for detecting volcanic plumes and clouds using the IR multispectral instruments mentioned above is BT [29,33]. The brightness temperature of the two bands, located at wavelengths of 11–12 μm for ash and at 7.3 and 8.7 μm for SO₂, were used to discriminate between volcanic and meteorological clouds, allowing for detection and monitoring. The BT is also used for quantitative retrievals of the total ash mass, effective radius, and aerosol optical depth (AOD) to retrieve these parameters (a microphysical model is used in conjunction with brightness temperatures measured at 11 and 12 μm [80,81]). To perform these calculations, simulated top-of-atmosphere (TOA) radiances are generated using a radiative transfer model (RTM) [12]. The TOA-simulated radiances are computed based on atmospheric profiles (pressure, temperature, and humidity—PTH), surface characteristics (temperature and emissivity), volcanic plume geometry (plume altitude and thickness), and the optical properties of volcanic ash by setting a threshold. The RTM can also be used to compute lookup tables (LUTs) [11,47,52,55,70], which are commonly used for retrieval.

Another method used to analyze IR data is volcanic plume retrieval (VPR), a technique created to extract the SO₂ mass, effective radius, and optical depth of a volcanic cloud from its thermal radiation at 8.7, 11, and 12 μm [47,52,55]. It stands out for its simplicity of use and computational speed, which make it particularly effective for monitoring. It is based on the estimation of a virtual picture that represents what the sensor would have observed in a multispectral thermal image if a volcanic cloud were not present. As soon as new satellite images of an eruption become available, the VPR technique may provide updated estimates of ash and SO₂ with plume temperature as an extra input. A new atmospheric

model for estimating cloud transmittance was introduced by Pugnaghi et al. [55], which improved the percentage difference between the average input data of the synthetic images and the mean results of the VPR from 4 and 68% to 0 and 21%, respectively.

Other methods developed for ash cloud detection have shown excellent results. Robust satellite techniques (RSTs) are a multi-temporal data analysis approach that considers every anomaly in the space–time domain as a deviation from an “undisturbed” state, specific for each location and time of observation in specific [31,32,36,37,46]. RST has a success rate of 90.1% for ash detection when applied to polar orbit instruments, such as AVHRR and MODIS [37], geostationary instruments, such as SEVIRI and AHI, and data from out-of-service MTSAT-1R and MTSAT-2 imagers [31,32,46]. Although these methods strongly rely on BTM, they overcome the limitations of defining fixed thresholds as in traditional methods. The application of principal component analysis (PCA) [30,51,73] to MODIS data has also shown good results [30,51].

Stereo techniques [40,41,45,54,75] have also been applied for plume height retrieval. Scollo et al. [40] used MISR and analyzed the data using MINX software to retrieve plume heights with uncertainties of <500 m. The MISR stereo plume heights in Ekstrand et al. [45] were compared with traditional BTM method height retrievals. This comparison between the results from the ash dispersion models and aircraft gas flight data confirmed that radar and MISR stereo heights are more accurate than basic satellite temperature heights. The main limitation of applying MISR data is the low temporal resolution of this instrument with a 9-day revisit time. It uses several cameras to examine the Earth’s surface from various angles, allowing for the extraction of 3D data despite its stereo-viewing capacity, which is restricted to specified viewing angles.

More recently, procedures applying machine learning, such as that of Piontek et al. [76], developed a new ash retrieval method using artificial neural networks (ANNs) with an ash detection probability of >90%. Similar results show the benefits of adding machine learning to the retrieval procedures using neural networks (NNs) and a support vector machine (SVM), allowing for an automatic and less time-consuming process and reducing the error of attributing a fixed temperature threshold with accuracy for ash detection > 85% [77,79].

For SO₂ retrievals in the IR region, IASI and AIRS showed great sensitivity in retrieving heights above 5 km, even for low vertical column densities of 1 dobson unit (DU). However, in the UV spectral band, susceptibility to SO₂ is higher at lower elevations, and the DOAS method has been widely applied, allowing fast retrieval. Other sensors, such as the OMPS-LP, can provide relatively high-vertical-resolution aerosol profiles from measurements of scattered solar radiation in the 290–1000 nm spectral range, allowing accurate height retrievals [78].

New strategies based on inverse learning machine schemes, developed by Efremenko et al. [59] for GOME-2 and, more recently, for TROPOMI and OMI, have increased computational efficiency over earlier methods, allowing near real-time retrievals with great accuracy. However, these sensors are highly affected by atmospheric conditions, which is a major limitation, particularly for large volcanic eruptions.

Theys et al. [13] developed the covariance-based retrieval algorithm (COBRA). COBRA is combined with an iterative LUT to apply TROPOMI measurements taken aboard the Sentinel-5 Precursor spacecraft, which has a spatial resolution of 3.5 × 5.5 km². TROPOMI captures locally enhanced SO₂ columns with a higher resolution than prior sensors such as the OMI. This technique addresses the nonlinear contribution of SO₂ to the measured signal, significantly reducing the spectral interference and retrieval noise. This combined retrieval technique improves the sensitivity of estimating both SO₂ vertical column density (VCD) and SO₂ layer height, eliminating the requirement for time-consuming online radiative transfer simulations.

4.2. B- Ground-Based Remote Sensing for Volcanic Plumes and Cloud Monitoring (n = 24)

Table 2 summarizes the articles included in the systematic review of the use of ground-based remote sensing approaches for detecting and monitoring volcanic clouds. The main

objective was to identify the most common ground-based instruments and methods for ash and SO₂ monitoring.

Table 2. Summary of articles related to ground-based remote sensing for volcanic cloud monitoring ($n = 24$).

Reference	Case Study	Data Source	Retrieval Method	Main Outcomes
[7]	Grímsvötn 2011	C-band and X-band weather radar	Rainbow 5 Software	Plume top height ≈ 20 (21 May 2011). $R^2 = 0.67$.
[82]	Etna 2010	VAMP LiDAR	Klett–Fernald and Polarization LiDAR technique	Ash concentration estimation with an uncertainty of 50%.
[83]	Etna 2010	VAMP LiDAR	Klett inversion	Plume height ≈ 5 km. Ash concentration = $\pm 24,000 \pm 6000$ mg/m ⁻³ . Systematic uncertainty of 50% on the retrieved value of mass concentration is related to an effective radius of 10 mm for ash.
[6]	Shinmoedake 2011	COMPUSS (USB2000 or USB2000+ spectrometers from Ocean Optics)	Differential optical absorption spectroscopy (DOAS) method	Total SO ₂ emission ≈ 280 kt. SO ₂ flux > 10,000 ton/day.
[84]	Grímsvötn 2011	Keflavík C-band weather radar	VARR methodology	Plume top height ≈ 20 . Mean MER $\approx 4.44 \times 10^{11}$.
[85]	Redoubt 2009	Doppler C-Band Radar (MM-250C)	Standard atmospheric refraction model	Plume top height ≈ 19 km (3/26/09).
[86]	Stromboli 2013	FLAME network of scanning UV spectrometers and SO ₂ camera monitoring system	Flux Automatic Measurement in real-time analysis	SO ₂ flux measured with SO ₂ camera agrees well with FLAME network.
[87]	Stromboli 2013, Karymsky 2011 & Lásçar 2012	NicAir IR Camera	Algorithm based on Temperature Difference and Optical flow method	Stromboli: Mean ash flux 53.0 ± 25.8 kg/s. Total fine ash emitted ≈ 4 t/SO ₂ masses ≈ 51 –160 kg. Karymsky: Ash cloud height > 2000 m (a.v)/Total fine ash mass >10 t/Fine ash Mass flux of ≈ 150 kg/s. Lásçar: SO ₂ mean flux ≈ 130 t day. Errors in fine ash SCDs in the range of 20–50%.
[88]	Etna 2011	Visible and thermal cameras and LiDAR	Klett–Fernald algorithm	Plume top height ≈ 8.5 – 9 ± 0.5 km (12 August 2011). Concentration of volcanic ash fixed to 2450 kg/m ³ with 55% of uncertainty.
[89]	Calbuco 2015	C-band INVAP S.E. Radar system (5.6 GHz)	Standard atmospheric refraction model	Plume top height $\approx 22.8 \pm 2.1$ km (a.s.l.).
[90]	Bárðarbunga 2014–15	UV-sensitive Ocean Optics Maya2000 Pro	DOAS Method	Post-eruption outgassing of SO ₂ = 3 ± 1.9 kg/s.
[91]	Pacaya 2011	Microtops-II Sun-Photometer	Background atmosphere Correction	AODs < 0.1.

Table 2. Cont.

Reference	Case Study	Data Source	Retrieval Method	Main Outcomes
[92]	Etna 2010–2011	Multi-Wavelength Raman LiDAR	VALR-ML methodology	Etna 2010: Ash average concentration is about $8.63 \pm 6.04 \text{ mg/m}^3$. Mean diameter is about $3.37 \pm 2.04 \text{ }\mu\text{m}$. Concentration uncertainty 40% up to 43% and mean diameter 7%. Etna 2011: Ash plume height = 6.5–8 km (a.s.l.). Average concentration is about $65.00 \pm 37.3 \text{ mg/m}^3$. Mean diameter is about $3.01 \pm 1.2 \text{ }\mu\text{m}$. VALR estimations with backscattering coefficient error of 50%.
[93]	Etna 2011–2015	L- Band Doppler Radar	VARR	Plume height 15 km (a.s.l.). MER from 2.96×10^4 to $3.26 \times 10^6 \text{ kg/s}$.
[94]	Fuego 2017	FLIR Photo n640 camera	Segmentation algorithm based on BTM, space carving algorithm, and Multiview 3D ash plume reconstruction	Plume height between 1000 m and >2000 m (a.v.). Volume between $2 \times 10^8 \text{ m}^3$ and $8 \times 10^8 \text{ m}^3$.
[95]	Calbuco 2015	C-band INVAP S.E. radar system (5.6 GHz)	Concept of Equivalent Sphere	Plume height = 25 km (a.s.l.). Total emission was $2.34 \times 10^{12} \text{ kg}$.
[96]	Etna 2015	FTIR single pixel and a UV camera	LATMOS Atmospheric Retrieval Algorithm (LARA) and DOAS ultraviolet spectroscopy	Underestimation of the SO ₂ slant column densities (SCDs) of the UV camera by a factor of 3.6.
[97]	Etna 2013	L- and X-band Doppler Radar	VARR methodology MER estimation using SFA, MCA, and TPA methodologies	TPA-DB12 = $4.3 \pm 1.0 \times 10^9 \text{ kg}$. TAO-MA09 = $1.7 \pm 0.4 \times 10^9 \text{ kg}$. SFA using TIC data = $4.7 \pm 1.3 \times 10^9 \text{ kg}$. SFA using L-band VDR = $4.2 \pm 1.0 \times 10^9 \text{ kg}$. MCA using X-band MWR and SFA using X-band MWR = $3.9 \pm 0.9 \times 10^9 \text{ kg}$.
[8]	Etna 2015	Hyper IR Camera	LATMOS Atmospheric Retrieval Algorithm (LARA)	Accuracy of the classification with $R^2 = 0.94$. SO ₂ flux error = 16%.
[98]	Yasur 2018	PiCam UV	Optimal flow method and PIVlab in MATLAB	SO ₂ fluxes ranged from 4 to 5.1 kg s^{-1} , uncertainty of -12.2% to $+14.7\%$.
[99]	Etna 2019	UV-sensitive CMOS sensor	Imaging Fabry–Pérot interferometer correlation spectroscopy (IFPICS)	SO ₂ mass flux of = $84 \pm 11 \text{ td}^{-1}$. Limit for the SO ₂ measurement is $5.5 \times 10^{17} \text{ molec. cm}^{-2\text{s}^{-1/2}}$.
[100]	Etna 2016	Dual-Wavelength Polarimetric LiDAR	VALR Maximum Likelihood (ML), Single Regressive (SR), and Multi-Regressive (MR)	VALR and ML ash concentrations $0.1 \text{ }\mu\text{g/m}^3$ and 1 mg/m^3 and particle mean sizes of $0.1 \text{ }\mu\text{m}$ and $6 \text{ }\mu\text{m}$, respectively. SR method differences are less than <10%.

Table 2. Cont.

Reference	Case Study	Data Source	Retrieval Method	Main Outcomes
[101]	Cumbre Vieja 2021	Micropulse LiDAR	Polarization LiDAR Photometer Networking (POLIPHON) algorithm	Plume height \approx 2.8 km (15 November). Highest ash load (18 October) with a range of $800\text{--}3200\mu\text{g m}^{-3}$. Ash backscatter coefficient, aerosol optical depth, volume, and particle depolarization ratios were, respectively, 3.6 (2.4) $\text{Mm}^{-1}\text{sr}^{-1}$, 0.52 (0.19), 0.13 (0.07), and 0.23 (0.13) on 18 October (15 November).
[102]	Cumbre Vieja 2021	CL51 and CL61 ceilometers (LiDAR) and AERONET sun photometers	Wavelet Covariance Transform (WCT) method	Plume height \approx 4 km (a.v.l). Ash mass concentration $313.7\mu\text{g m}^{-3}$.

Ground-based remote sensing allows for more precise vertical profiling of volcanic plumes as well as additional data and interaction with existing networks. However, it has limitations in terms of spatial coverage, weather dependency, field of view, and difficulties associated with inverse modeling, accessibility, and operational costs.

Three types of instruments are commonly used for ground-based remote sensing monitoring: ground-based weather radar and LiDAR [7,82–85,88,89,92,93,95,97,100–102], IR/UV cameras [8,86–88,94,96,98], and UV spectrometers [6,86,90,91,99,102].

LiDAR can perform direct measurements of plumes, allowing real-time monitoring of the changes in the optical properties of volcanic aerosols. Scollo et al. [82] developed a technique using a volcanic ash monitoring by polarization (VAMP) LiDAR system that allows the detection of elastic backscattering radiation at 532 nm using depolarization techniques for particle estimation. This technique accounts for uncertainties ranging from 40 to 50% in retrievals [83], despite its real-time monitoring capabilities. Another retrieval algorithm applied by Mereu et al. [92,100] is a physically based inversion methodology named volcanic ash LiDAR retrieval (VALR), based on the maximum likelihood (ML) and using dual-wavelength Raman LiDAR with robust results. The fundamental limitation of employing LiDAR technology is the signal degradation caused by optically dense cloud layers. However, this constraint is primarily related to massive explosive volcanic eruptions.

Marzano et al. [97] proposed and applied the volcanic ash radar retrieval (VARR) to S-, C-, L-, and X-band weather radars. The VARR technique, which uses a Bayesian classification and optimal regression algorithm, is based on the active tracer high-resolution atmospheric model (ATHAM) algorithm, a physical statistical methodology based on the backscattering microphysical model of volcanic particles (hydrometeors, ash, and aggregates).

In addition, UV spectrometers, such as the DOAS technique, are frequently employed for ground-based SO_2 flux and total mass monitoring. FLIR, hyperspectral IR, and UV cameras are other efficient remote sensing systems frequently used in networks, such as FLAME [86]. Segonne et al. [8] used hyperspectral IR photography, especially Hyper-Cam technology, to assess the SO_2 emission flux in near real-time from Etna. They created a classification system for IR hyperspectral images of volcanic plumes and used the “box method” to estimate SO_2 emission flux with 84% accuracy. Fuchs et al. [99] demonstrated the viability of quantitative imaging of volcanic SO_2 flux using imaging Fabry–Pérot interferometer correlation spectroscopy (IFPICS), which provides enhanced calibration and expanded field-measuring capabilities. Ilanko et al. [98] used UV cameras to assess explosive (Strombolian) gas masses and found links between gas production, conduit sealing, and intensity of explosions. Wood et al. [94] developed a proof of principle for reconstructing ash plumes utilizing NicAIR IR camera systems. This approach can be used

to discriminate ash plumes from the ground or background sky, with limits and possible sources of error.

4.3. C-Airborne/UAV-Based Remote Sensing for Volcanic Plumes and Cloud Monitoring ($n = 5$)

Table 3 summarizes the articles included in the systematic review regarding the use of airborne/UAV-based remote sensing approaches (data sources, retrieval methods, and main outcomes) for monitoring volcanic clouds.

Table 3. Summary of articles related to airborne/UAV-based remote sensing for volcanic cloud monitoring ($n = 5$).

Reference	Case Study	Data Source	Retrieval Method	Main Outcomes
[10]	Eyjafjallajökull 2010	FAAM Bae-146 airplane LiDAR and OPC	In situ airborne measurements of the ash cloud	Concentration of particles > 400 nm. Mass concentration 77 μgm^{-3} .
[103]	Ontake 2014	Multicopter UAV (α UAV series) with MultiGAS box (black box) InfReC G120EX, Nippon Avionics Co. Ltd., Japan	DOAS technique and plume sampling	SO ₂ flux > 2000 t/d at least until 20 h after the eruption.
[104]	Fuego 2018	RiteWing Zephyr II Skywalker X8	Secondary Electron Microscopy (SEM) ash collection	Appropriate collection mechanism, aerial sampling of ash, with a representative PSD from within a plume.
[105]	Stromboli	sUAV with a 4k camera	Interaction between motors and ash	Interactions with fine ash < 250 μm motor blockage happened.
[9]	Yasur 2018	DJI Phantom-3 UAV	Photogrammetry	Plume volume $\sim 3430 \text{ m}^3 \pm 512 \text{ m}^3$.

In situ (eruption site) airplane observations are appropriate for comprehensive ash measurements of the particle size distribution (PSD) and concentration [10]. UAV-based approaches [103,104] are advantageous for monitoring volcanic plumes from close and secure distances, particularly in remote or hazardous locations. Furthermore, these approaches allow for effective sample collection mechanisms (e.g., aerial sampling of ash with a representative plume PSD). Photogrammetry provides geographical information and 3D modeling of volcanic plumes [9]. However, all these approaches have limitations and must be carefully selected according to the research aims and restrictions of the study area. Brosch [105] analyzed the stress factors associated with the deployment of UAVs in volcanic areas, such as strong winds, high temperatures, incandescent volcanic particles, and corrosive gases in the atmosphere.

4.4. D-Multiplatform Approaches for Volcanic Plumes and Cloud Monitoring ($n = 9$)

Table 4 summarizes the articles included in the systematic review of the use of multiplatform remote sensing-based approaches (study cases, data sources, retrieval methods, and main outcomes) for monitoring volcanic clouds. As demonstrated above, satellite observations provide extensive geographical coverage and long-term monitoring capabilities. However, there are drawbacks, including the lack of high spatial resolution and difficulties in distinguishing between different volcanic plumes [106].

Table 4. Summary of articles related to multiplatform approaches for volcanic cloud monitoring ($n = 9$).

Reference	Case Study	DATA SOURCE	Retrieval Method	Main Outcomes
[106]	Okmok 2008	CALIOP, OMI, and MFDOAS	LF algorithm, offline ISF, and DOAS technique	Plume heights $\approx 11.5 \text{ km} \pm 1.5 \text{ km}$. Vertical column density (VCD) = $1.75 \pm 0.16 \text{ DU}$ and $1.22 \pm 0.18 \text{ DU}$ (OMI) $3.11 \pm 0.23 \text{ DU}$ (DS-MFDOAS) (SO_2). Total erupted mass (SO_2) $\approx 0.6 \text{ Tg}$ (OMI).
[16]	Kasatochi 2008	CABRIC DOAS instrument and GOME-2	DOAS technique, Monte Carlo Atmospheric Radiative Transfer and Inversion Model (McArtim)	$R^2 = 0.84$ (SO_2 vertical column by GOME-2 vs. averaged CARIBIC values). Plume heights $\approx 11 \text{ km}$. VCD $\approx 3 \times 10^{17} \text{ molec/cm}^2$ (SO_2). Total erupted mass (SO_2) $\approx 1.5\text{--}2.5 \text{ Tg}$.
[107]	Etna 2006	UV Scanner DOAS (FLAME NETWORK), MODIS IASI	BT, MODTRAN (RTM), and DOAS technique	$R^2 = 0.87$ (6 of December). SO_2 flux $\approx 6700 \text{ t/d}$ (FLAME SO_2) and $\approx 5800 \text{ t/d}$ (MODIS SO_2) 6 of December.
[108]	Etna 2011	MODIS, IASI, GOME-2, and UV Scanner DOAS (FLAME NETWORK)	IASI-UNIOX algorithm, ULB algorithm MODIS least square fit, and RAL product based on the Optimal estimation	FLAME SO_2 mass = 4.5 Gg. Differences for satellite: MODIS = 10%; IASI = 15%; GOME-2 = 30%. SO_2 flux correlation coefficient between MODIS and FLAME is 0.84.
[109]	Holuhraun 2014	OMI, OMPS, and Brewer spectrophotometer	PCA, BRD, and LF	Brewer SO_2 total column record value = 13.9 DU. 6 September SO_2 columns are 2.59 DU from BRD algorithm and 2.79 DU for PCA with great agreement, while the Brewer measurement gives 4.4 DU.
[110]	Etna 2013	SEVIRI, MODIS, IASI, DPX4, and Camera	VPR (SEVIRI), VARR (DPX4), BT (MODIS/SEVIRI), and Optimal estimation with RTTOV (IASI)	1–2% of total ash was airborne. Plume heights up to 12.6 km. Ash mass retrieval maximum difference before and after the multisensor approach is about 40%.
[111]	Etna 2011/2013	SEVIRI and VIVOTEK IP8172P	BT of the coldest pixel with the atmospheric temperature profile and Visual methods	Plume height of 15 km (a.s.l.). Uncertainty of the plume height was set to $\pm 500 \text{ m}$.
[112]	Etna 2011	VOLDORAD-2B (V2B) scanning microwave weather radar (MWR), SEVIRI MODIS, and IR Camera	ECV, SFA, NSA, TPA, MCA, VPR-ash, and VPR-ICE	2011 (Average MER): V2B = $3.1 \pm 0.7 \times 10^5$; MWR = $1.7 \pm 0.6 \times 10^6 \text{ kg/s}$; IR Camera = $7.5 \pm 4.7 \times 10^5 \text{ kg/s}$; SEVIRI = $2.7 \pm 2.5 \times 10^4 \text{ kg/s}$; MODIS = $2.6 \pm 3.1 \times 10^2 \text{ kg/s}$. 2012 (Average MER): V2B = $1.5 \pm 1.3 \times 10^5 \text{ kg/s}$; MWR = $1.4 \pm 0.9 \times 10^5 \text{ kg/s}$; IR Camera = $8.6 \pm 2.5 \times 10^4 \text{ kg/s}$; SEVIRI = $1.4 \pm 1.8 \times 10^6 \text{ kg/s}$; MODIS = $2.6 \pm 3.1 \times 10^2 \text{ kg/s}$.
[15]	Etna 2020 to 2022	INGV-OE monitoring system	GNSS, Infrasonic Stations, UV scanners, and VIS/IR cameras	Maximum plume heights (a.s.l.): 13–14 December 2020 = 5.5 km; 28 February 2021 = 12.6 km; 12 March 2021 = 9 km.

Merucci et al. [107] used ground-based observations with satellite retrievals, with results presenting correlations of $R^2 = 0.87$ for SO_2 flux measurements. This approach proved that the reconstruction of SO_2 fluxes is possible with MODIS data when ground-based monitoring is unavailable.

Aircraft measurements include those using the Civil Aircraft for the Regular Investigation of the Atmosphere Based on an Instrument Container (CARIBIC) flying observatory DOAS instrument and GOME-2 satellite data. They give extra insights and support satellite observations with $R^2 = 0.84$ (SO_2 vertical column observed by GOME-2 vs. averaged CARIBIC values). However, their availability is limited, and it is possible that they do not fully reflect the spatial extent of volcanic emissions [16].

As mentioned by Corradini et al. [15,93,106,110], multisensor techniques require a combination of data from several platforms and equipment. These techniques allow a better understanding of volcanic emissions, eruption dynamics, and source characteristics. Complete and reliable datasets were obtained by successfully integrating satellite observations, ground-based networks, and aircraft measurements, thus compensating for the shortcomings of individual techniques. Among other characteristics, tephra fallout, eruption mass discharge rate, and plume height have all been accurately assessed using multisensor techniques, with an improvement in results of the order of 40%.

Several studies (e.g., [15,106,111,112]) have demonstrated the value of merging satellite retrievals with ground-based networks to confirm and improve the precision of SO_2 measurements and near real-time tephra fallout assessments.

Overall, the accuracy and reliability of volcano monitoring can be significantly improved by integrating multiplatform remote sensing systems, including satellite observations, ground-based networks, aircraft measurements, and multisensor approaches. By overcoming the shortcomings of individual strategies, these approaches offer a thorough and in-depth understanding of volcanic emissions, eruption dynamics, and the associated volcanic hazards.

4.5. E-Remote Sensing Data Assimilation into Numerical Forecasting Models ($n = 28$)

Table 5 summarizes the articles included in the systematic review of remote sensing data assimilation into numerical forecasting models. These studies focused on the application of various VATDMs and instruments to analyze volcanic ash and SO_2 dispersal and their impact, compare satellite, ground-based, and UAV/aircraft data with numerical simulations, validate models with field data, improve volcanic ash predictions, increase the understanding of eruption dynamics, and assess the transport of volcanic aerosols over long distances.

Table 5. Summary of articles related to remote sensing data assimilation into numerical forecasting models ($n = 28$).

Reference	Case Study	Data Source	Retrieval Method	Main Outcomes
[113]	Etna 2001 & 2002	MIRS and FALL3D Model	MINX V1.0 Software and Bouyant Plume Theory (BPT)	Plume height ≈ 5 km (23/07/2001) and 6 km (2002).
[18]	Kasatochi 2008 & Okmok 2008	OMI, MFDOAS, AVHRR, and MLDP0 Model	LF algorithm, offline ISF, and DOAS technique and BT method	SO_2 concentration = SO_2 —8.7 DU (18 July); 5.8 DU (19 July). Plume heights ≈ 10 –16 km.
[114]	Etna 2002	MODIS and FALL3D	BTD and MODRAN (RTM)	MODIS total ash mass ≈ 20 to 45 kt. FALL3D total ash mass ≈ 35 to 60 kt. Mean AOD $\approx 0.8 \mu\text{m}$. Good agreement in the first 300 km. Retrieval errors = 40% and 30% for total ash mass and mean AOD.

Table 5. Cont.

Reference	Case Study	Data Source	Retrieval Method	Main Outcomes
[115]	Eyjafjallajökull 2010	Three-dimensional Eulerian Chemistry Transport Model (CMAQ), AERONET Network DRL falcon	Comparison between model AOD and AERONET AOD	Agreement was achieved for lower emission heights.
[116]	Grímsvötn 2011	C-band weather radar and ATHAM Model	VARR	The results show a good agreement between simulations and measurements.
[117]	Eyjafjallajökull 2010	NAME Model and FAAN Bae-146	Comparison between PSD Aircraft and NAME simulations	On 5 May, quantitative agreement between NAME simulations and observations for particles with diameters between 10.0 and 30.0 μm .
[118]	Eyjafjallajökull 2010	IASI and CHIMERE Model	BTD	Inversion procedure combining IASI satellite observations and CHIMERE allows reconstruction of the SO_2 flux.
[119]	Chaitén 2008	MODIS and FALL3D Model	BTD	Agreement between simulations and observations; differences result from model.
[120]	Eyjafjallajökull 2010	MERIS, ASTER, and VOL-CALPUFF Model	Shadow Technique and BTD and RTM	Plume heights 5–10 km. Retrieved remote sensing data and model reliable up to a scale of hundreds of kilometers, showing good agreement.
[121]	Grímsvötn 2011	IASI and FLEXPART Model	Inversion Method	SO_2 emission = 0.61 ± 0.25 Tg. Fina ash emission = 0.49 ± 0.1 Tg. Diameter = 2–28 μm Simulation bias = 44%.
[122]	Kelut 2014	AHI and CALIOP FLEXPART	BTD	Most ash injected into 16–17 km. Modelled volcanic concentrations = 9 ± 3 mg m^{-3} .
[123]	Ruapehu 1996	GOES-9 and FLEXPART-WRF Models	BTD method	Plume ratio had a large effect on the model. Uncertainties of plume height do not have a significant impact on the model. The model performance is strongly dependent on the meteorological model.
[124]	Kasatochi 2008	MODIS, CALIOP, and HYSPLIT Model	BTD method	MER calculated from observations: $\text{MER}_{\text{fine}} = 2.8 \times 10^4$ kg s^{-1} ; $\text{MER}_{\text{fine}} = 2.8 \times 10^3$ kg s^{-1} ; $\text{MER}_{\text{fine}} = 2.8 \times 10^5$ kg s^{-1} ; $\text{MER}_{\text{fine}} = 2.8 \times 10^6$ kg s^{-1} .
[125]	Kelut 2014	AHI and HYSPLIT Model	BTD and Geostationary Cloud Algorithm Testbed (GEOCAT)	Very good qualitative agreement between forecast and satellite observations of BT, BTD, and ash probability provided by GEOCAT.
[126]	Grímsvötn 2011	SEVIRI and NAME Model	BTD	Clouds led to an average 6 to 12% reduction detection of ash. Simulations are in very good agreement with observations.
[127]	Sakurajima 2019	X-band MP Radar and PUFF Model	Parallax-based method and the Plume Elevation Model (PEM)	Plume top 4 to 5.5 km (a.s.l.). Total ash emission was 8800 tons. Use of PUFF combined with MP radar data provides accurate results.

Table 5. Cont.

Reference	Case Study	Data Source	Retrieval Method	Main Outcomes
[128]	Kasatochi 2008	MODIS, CALIOP, and HYSPLIT Model	Four-channel Algorithm	It is found that the emission estimates vary significantly with different variations in observations inputs.
[129]	Kamchatka & Kurilc Islands	MODIS and PUFF Model	VolSatView	A new tool developed for solving the problems of integrated monitoring of ash cloud transport.
[130]	Etna 2013	AERONET network, SEVIRI, and FALL3D Model	BTD and LUT and Field data	Plume height ≈ 8.7 km (a.s.l.). TEM of $\approx 4.9 \times 10^9$ kg. MER of $\approx 1.3 \times 10^6$ kg/s.
[131]	Merapi 2010–11	AIRS, MIPAS, and MPTRAC Model	MIPAS altitude-resolved aerosol cloud index (ACI) and Aerosol Index (AI) and AIRS-optimized SO ₂ index based on BT algorithm	Merapi sulfur contribution of 8800 t to Antarctic lower stratosphere.
[132]	Etna 2013	SEVIRI, MODIS, Rada, IR Cameras, FPlume, and FALL3D Models	Integration of field, radar, and satellite TGSD to inversion results with FALL3D	Inversion TGSD yield 75 wt% of field data, 25 wt% of radar. Best matching PM ₂₀ for SEVIRI was from 3 to 6 to 9.0 wt%.
[133]	Fuego 2018	IASI, PlumeTraj, and Plume-MoM Models	Elementary radiative transfer and a large lookup table (detailed in [134])	≈ 2 h 50 m climatic paroxysmal phase MER ≈ 1.4 kg s ⁻¹ . Plume estimates 0.03 ± 0.004 km ³ . SO ₂ emission ≈ 130 Kt.
[135]	Puyehue-Cordón Caulle 2011	MODIS and HYSPLIT Model	Geostatistical treatment of BTD results and HYSPLIT back-trajectory	Back trajectory accuracy of 80% within 60 km of the source volcano.
[136]	Etna 2018	SEVIRI and Plume-Mom and HYSPLIT Models	Ensemble square root Kalman Filters (EnSRKFs) and VPR	Accurate knowledge of ESPs is not mandatory for model initialization with the use of EnKFs for ash forecasting.
[137]	Copahue 2016	OMI, HYSPLIT Model	Aerosol Index from OMPS and OMI SO ₂ Algorithm	Good agreement between HYSPLIT SO ₂ concentrations and OMPS AI estimations.
[138]	Barren 2018	Sentinel-2, MODIS, OMI LISS-IV, and HYSPLIT	MIROVA algorithm	Combination of sensor observations with HYSPLIT proven effective.
[17]	Raikoke 2019	FPlume Model and Himawari	ICAN-ART integration with FPlume	Reduction of mass overestimation from 37% to 18%. Simulated spatial dispersion of the ash and SO ₂ agrees well with Himawari-8 as our SAL analysis.
[139]	Etna 2013	V2B Radar, OMPS, VIIRS, SEVIRI, and WRF-CHIMERE	WRF-Chem model configured with eruption source parameters (ESPs) obtained elaborating the raw data from the VOLDORAD-2B (V2B) Doppler radar system	Good comparison with satellite retrievals.

A number of VATDMs such as Numerical Atmospheric-dispersion Modelling Environment (NAME) [117,126], Modèle Lagrangien de Dispersion de Particules d'ordre zéro (MLDP0) [18], FALL3D [113,114,119,132], CMAQ [115], Hybrid Single Particle Lagrangian Integrated Trajectory (HYSPLIT) [124,125,128,135,136], PUFF [129], Massive-Parallel Trajectory Calculations (MAPTRAC) [131], VOLC-CALL PUFF [120], PlumeTraj [133], PlumeMoM [133],

chemistry transport model (CHIMERE) [118,139], and Fplume [17] have been used in conjunction with MISR, MODIS, SEVIRI, IASI, OMI, VIIRS, OMPS, AIRS, ABI, and AHI satellite data, ground-based data [116,129,133,136,139], and UAV/aircraft-based remote sensing data [117].

When comparing MISR data with numerical simulations of three-dimensional volcanic aerosol dispersal using the FALL3D model, fluctuations in estimations were observed when modifications in input data were performed [113], demonstrating the importance of retrieving accurate data to input in dispersal models. A comparison between FALL3D and satellite sensors was also performed using MODIS retrievals of ash clouds, and good agreement was found between the retrieved data and simulation in the first 300 km from the vent [114]. Boichu et al. [118] also used satellite retrievals with CHIMERE to account for volcanic SO₂ flux at a high temporal resolution for the 2010 Eyjafjallajökull eruption. For instance, Crawford et al. [124] used satellite images of volcanic ash from the 2008 Kasatochi eruption to apply to HYSPLIT, while Wilkins et al. [126] used a data insertion update strategy for the NAME model ash transport during the 2011 Grímsvötn eruption.

Ensemble-based data assimilation has also been used to minimize uncertainties and enhance projections. Pardini et al. [136] used the HYSPLIT model to perform ensemble-based data assimilation of volcanic ash clouds from satellite observations and found that accurate knowledge of ESP is not mandatory for model initialization with the use of Ensemble Kalman Filters (EnKFs) for ash forecasting.

In addition to these studies, Tanaka et al. [127] employed the PUFF model to estimate volcanic ash plume dispersal for Sakurajima in 2019 using MP radar observations, resulting in accurate results. Whereas Paez et al. [137] investigated volcanic SO₂ and ash emissions with good agreement between HYSPLIT SO₂ concentrations and OMPS Aerosol Index estimations, Gunda et al. [138] used HYSPLIT and satellite observations to model Sentinel-2, MODIS, and OMI data. Using ground and satellite remote sensing data, Rizza et al. [139] investigated the effects of variable ESP on volcanic plume transport during the 23 November 2013 paroxysm event of Etna. The study of Bruckert et al. [17] demonstrated that the online treatment of eruption dynamics enhanced the forecasting of volcanic ash and SO₂ dispersion for the 2019 Raikoke.

Utilizing remote sensing data in conjunction with models can significantly improve the accuracy and understanding of volcanic processes, thereby enabling the detection of volcanic clouds and a more precise estimation of the initial eruptive parameters. This, in turn, enhances volcanic dispersion models and facilitates decision-making procedures during volcanic eruption operations.

5. Conclusions

The scientific community is highly knowledgeable about using remote sensing technologies to detect and monitor volcanic plumes and clouds. Various instruments, including those on polar or geostationary satellites and ground-based platforms, such as radar, thermal cameras, LiDAR, UAVs, and airplanes, can be used to measure the physical parameters of volcanic ash and SO₂.

Satellite detection methods are the most commonly used methods for the detection and monitoring of volcanic clouds. This is due to the abundance of available sensors that can obtain data every 10 or 15 min (AHI, SEVIRI, and ABI) or daily (MODIS, TROPOMI, and IASI). However, the methods used to identify ash and SO₂ and obtain their physical parameters have certain limitations. One of the main limitations of IR methods is determining a fixed temperature threshold to discriminate between volcanic clouds and atmospheric clouds, which introduces significant uncertainty into traditional methods such as BTD when cloud coverage is extreme or when the cloud is opaque. One method that can reduce this limitation is RSTash, which produces detection rates of >90% and provides a solution that uses a dynamic threshold for temperature in the retrieval procedure. Computational methods, such as statistical methods, neural networks, and deep learning algorithms (PCA and VACOS algorithms), can also reduce this limitation by eliminating the need to identify

fixed threshold values. These methods can decrease missed detection and operator error during data processing. Still, they are limited only by the amount of data available for training and the limitations associated with the sensor used to retrieve data. With the growing amount of available data and the launch of new sensors with better resolution, these methods have been shown to perform better and have the capacity to replace the traditional methods.

Determining the height of volcanic plumes is one of the most important parameters for estimating MER. However, this presents a significant challenge for IR sensors owing to temperature inversion at tropopause or plume undercooling [65]. The stereoscopic methods used in MISR, GOES, and SEVIRI produced good results, with a small error compared to the temperature difference method.

UV hyperspectral sensors, such as TROPOMI, demonstrate an unrivaled capability for SO₂ retrieval, and the results are even more promising when combined with the new COBRA algorithm, which reduces scattering and noise and improves detection accuracy. However, one of its major limitations is scattering during cloudy weather, which precludes accurate measurement.

Despite their numerous advantages, satellites have limitations. As discussed above, most retrievals are made with high-temporal-resolution EO satellites to enable near real-time data acquisition, which decreases the accuracy owing to the lower spatial resolution, and the optical properties of each sensor are limited. Satellites with higher spatial resolutions, such as CALIOP and MISR, have low temporal resolutions of 16 and 9 days, respectively. For example, when CALIOP data are available, they can be used to validate the other methods.

Ground-based approaches using radar and LiDAR are well suited for providing near real-time retrievals and complementing satellite data. In addition, networks of UV spectrometers and IR/UV hyperspectral cameras such as FLAME and TIR camera systems are crucial for the real-time monitoring of SO₂ and ash retrievals. However, they also have limitations: cameras and spectrometers are affected by weather conditions and are limited by their field of view. Radar and LiDAR instruments also have limitations despite providing a better resolution than satellites for PSD. Radar reflectivity is limited by the shape of the particles and composition within the cloud, and they show limitations in providing cloud top heights, owing to the complex vertical structure of volcanic clouds. In addition, ground instruments that require maintenance are limited to the locations where they are installed and have significant acquisition costs.

Airborne/UAV-based approaches can be used to directly sample particles from volcanic clouds and provide precise PSD data. The limitations of these approaches include the instrument payload capacity, flying range, atmospheric conditions, and cost associated with the equipment, even if it is lower than that of other methods [104].

Although the reviewed studies have shown that the use of remote sensing is successful during eruptions for the detection and monitoring of volcanic clouds, combining various approaches is important for a better understanding of the volcanic ash dispersal dynamics. When data are available, multiplatform approaches show the best results, overcoming limitations intrinsic to each sensor and method and improving accuracy.

Numerical forecasting models play a crucial role in volcanic hazard management and are used operationally by VAACs in conjunction with remote sensing techniques. The assimilation of remote sensing data into VATDM has shown promising results for improving volcanic ash forecasting. However, further research is needed to develop more advanced data assimilation methods that can effectively combine various sources of remote sensing data with model simulations and accurately compare observations with simulation results.

The fine-scale dynamics of volcanic ash clouds can be better understood by improving the resolution of VATDM, which, together with remote sensing, can be a powerful tool for the assessment of their impacts, including aviation safety evaluations. Underestimation issues can be addressed using high-resolution modeling and enhanced satellite retrieval. Future research should concentrate on integrating various remote sensing techniques, such

as combining satellite thermal infrared data with radar or thermal infrared camera observations, when available, overcoming the spectral limitations of singular sensors, helping to characterize the physical properties of volcanic ash better, and improving the accuracy of ash cloud detection and tracking. Additionally, satellite data can be used to retrieve ash optical properties, and geostationary systems can be employed to monitor volcanic degassing, such as sulfur dioxide emissions. The absence of research addressing the impact of wind shear on volcanic cloud dispersion, and the potential for more effective identification of volcanic clouds from atmospheric clouds, was identified as a gap. It is known that the transport of volcanic particles is largely influenced by winds within the troposphere and/or stratosphere, with a particular emphasis on vertical wind shear [140,141]. Wind shear has been demonstrated to enhance the accuracy of simulations when it is taken into account [142].

The continuous evolution of remote sensing equipment with better resolution and faster acquisition time (e.g., GOES-18 and Meteosat third generation), will allow for the improvement in existing applications and the development of new approaches and enable the continuous monitoring of remote and difficult-to-access regions where ground monitoring systems are scarce or non-existent.

Supplementary Materials: The following supporting information can be downloaded at: <https://www.mdpi.com/article/10.3390/rs16101789/s1>, Excel file with article data.

Author Contributions: Conceptualization, R.M. and A.G.; methodology, R.M. and A.G.; data prospecting, analysis, and curation, R.M.; writing—original draft preparation, R.M.; writing—review and editing, A.G., A.P. and J.M.P. All authors have read and agreed to the published version of the manuscript.

Funding: This research was supported and funded by the Rui Mota grant from *Fundação para a Ciência e Tecnologia* (IU/BD/153514/2022), and by the IVAR grant from *Fundação para a Ciência e Tecnologia* (UIDP/00643/2020, DOI: 10.54499/UIDP/00643/2020).

Data Availability Statement: The data used in this work are freely and openly available in the Supplementary Material.

Conflicts of Interest: The authors declare no conflicts of interest.

References

1. Carey, S.; Bursik, M. Chapter 32—Volcanic Plumes. In *The Encyclopedia of Volcanoes*, 2nd ed.; Sigurdsson, H., Ed.; Academic Press: Amsterdam, The Netherlands, 2015; pp. 571–585, ISBN 978-0-12-385938-9.
2. Bonadonna, C.; Costa, A.; Folch, A.; Koyaguchi, T. Chapter 33—Tephra Dispersal and Sedimentation. In *The Encyclopedia of Volcanoes*, 2nd ed.; Sigurdsson, H., Ed.; Academic Press: Amsterdam, The Netherlands, 2015; pp. 587–597, ISBN 978-0-12-385938-9.
3. Prata, A.J.; Barton, I.J.; Johnson, R.W.; Kamo, K.; Kingwell, J. Hazard from Volcanic ASH. *Nature* **1991**, *354*, 25. [[CrossRef](#)] [[PubMed](#)]
4. Tupper, A.; Itikarai, I.; Richards, M.; Prata, F.; Carn, S.; Rosenfeld, D. Facing the Challenges of the International Airways Volcano Watch: The 2004/05 Eruptions of Manam, Papua New Guinea. *Weather Forecast.* **2007**, *22*, 175–191. [[CrossRef](#)]
5. Wilson, T.M.; Stewart, C.; Sword-Daniels, V.; Leonard, G.S.; Johnston, D.M.; Cole, J.W.; Wardman, J.; Wilson, G.; Barnard, S.T. Volcanic Ash Impacts on Critical Infrastructure. *Phys. Chem. Earth Parts A/B/C* **2012**, *45–46*, 5–23. [[CrossRef](#)]
6. Mori, T.; Kato, K. Sulfur Dioxide Emissions during the 2011 Eruption of Shinmoedake Volcano, Japan. *Earth Planets Space* **2013**, *65*, 573–580. [[CrossRef](#)]
7. Petersen, G.N.; Bjornsson, H.; Arason, P.; von Löwis, S. Two Weather Radar Time Series of the Altitude of the Volcanic Plume during the May 2011 Eruption of Grimsvotn, Iceland. *Earth Syst. Sci. Data* **2012**, *4*, 121–127. [[CrossRef](#)]
8. Segonne, C.; Huret, N.; Payan, S.; Gouhier, M.; Catoire, V. A Spectra Classification Methodology of Hyperspectral Infrared Images for Near Real-Time Estimation of the SO₂ Emission Flux from Mount Etna with LARA Radiative Transfer Retrieval Model. *Remote Sens.* **2020**, *12*, 4107. [[CrossRef](#)]
9. Gomez, C.; Kennedy, B. Capturing Volcanic Plumes in 3D with UAV-Based Photogrammetry at Yasur Volcano—Vanuatu. *J. Volcanol. Geotherm. Res.* **2018**, *350*, 84–88. [[CrossRef](#)]
10. Turnbull, K.; Johnson, B.; Marengo, F.; Haywood, J.; Minikin, A.; Weinzierl, B.; Schlager, H.; Schumann, U.; Leadbetter, S.; Woolley, A. A Case Study of Observations of Volcanic Ash from the Eyjafjallajökull Eruption: 1. In Situ Airborne Observations. *J. Geophys. Res. Atmos.* **2012**, *117*, D00U12. [[CrossRef](#)]

11. Corradini, S.; Merucci, L.; Prata, A.J.; Piscini, A. Volcanic Ash and SO₂ in the 2008 Kasatochi Eruption: Retrievals Comparison from Different IR Satellite Sensors. *J. Geophys. Res. Atmos.* **2010**, *115*, D00L21. [[CrossRef](#)]
12. Karagulian, F.; Clarisse, L.; Clerbaux, C.; Prata, A.J.; Hurtmans, D.; Coheur, P.F. Detection of Volcanic SO₂, Ash, and H₂SO₄ Using the Infrared Atmospheric Sounding Interferometer (IASI). *J. Geophys. Res. Atmos.* **2010**, *115*, D00L02. [[CrossRef](#)]
13. Theys, N.; Lerot, C.; Brenot, H.; van Gent, J.; De Smedt, I.; Clarisse, L.; Burton, M.; Varnam, M.; Hayer, C.; Esse, B.; et al. Improved Retrieval of SO₂ Plume Height from TROPOMI Using an Iterative Covariance-Based Retrieval Algorithm. *Atmos. Meas. Tech.* **2022**, *15*, 4801–4817. [[CrossRef](#)]
14. Webster, H.N.; Thomson, D.J.; Johnson, B.T.; Heard, I.P.C.; Turnbull, K.; Marenco, F.; Kristiansen, N.I.; Dorsey, J.; Minikin, A.; Weinzierl, B.; et al. Operational Prediction of Ash Concentrations in the Distal Volcanic Cloud from the 2010 Eyjafjallajökull Eruption. *J. Geophys. Res. Atmos.* **2012**, *117*, D00U08. [[CrossRef](#)]
15. Calvari, S.; Biale, E.; Bonaccorso, A.; Cannata, A.; Carleo, L.; Currenti, G.; Di Grazia, G.; Ganci, G.; Iozzia, A.; Pecora, E.; et al. Explosive Paroxysmal Events at Etna Volcano of Different Magnitude and Intensity Explored through a Multidisciplinary Monitoring System. *Remote Sens.* **2022**, *14*, 4006. [[CrossRef](#)]
16. Heue, K.P.; Brenninkmeijer, C.A.M.; Wagner, T.; Mies, K.; Dix, B.; Friess, U.; Martinsson, B.G.; Slemr, F.; van Velthoven, P.F.J. Observations of the 2008 Kasatochi Volcanic SO₂ Plume by CARIBIC Aircraft DOAS and the GOME-2 Satellite. *Atmos. Chem. Phys.* **2010**, *10*, 4699–4713. [[CrossRef](#)]
17. Bruckert, J.; Hoshyaripour, G.A.; Horváth, A.; Muser, L.O.; Prata, F.J.; Hoose, C.; Vogel, B. Online Treatment of Eruption Dynamics Improves the Volcanic Ash and SO₂ Dispersion Forecast: Case of the 2019 Raikoke Eruption. *Atmos. Chem. Phys.* **2022**, *22*, 3535–3552. [[CrossRef](#)]
18. D'Amours, R.; Malo, A.; Servranckx, R.; Bensimon, D.; Trudel, S.; Gauthier-Bilodeau, J.P. Application of the Atmospheric Lagrangian Particle Dispersion Model MLDP0 to the 2008 Eruptions of Okmok and Kasatochi Volcanoes. *J. Geophys. Res. Atmos.* **2010**, *115*, D00L11. [[CrossRef](#)]
19. Mastin, L.G.; Guffanti, M.; Servranckx, R.; Webley, P.; Barsotti, S.; Dean, K.; Durant, A.; Ewert, J.W.; Neri, A.; Rose, W.I.; et al. A Multidisciplinary Effort to Assign Realistic Source Parameters to Models of Volcanic Ash-Cloud Transport and Dispersion during Eruptions. *J. Volcanol. Geotherm. Res.* **2009**, *186*, 10–21. [[CrossRef](#)]
20. Monitoring VolCANiC ASH froM SPACE. 2010. Available online: https://elib.dlr.de/67813/1/STM-280_ash101004_V2.pdf (accessed on 17 May 2020).
21. Labazuy, P.; Gouhier, M.; Harris, A.; Guéhenneux, Y.; Hervo, M.; Bergès, J.C.; Fréville, P.; Cacaault, P.; Rivet, S. Near Real-Time Monitoring of the April-May 2010 Eyjafjallajökull Ash Cloud: An Example of a Web-Based, Satellite Data-Driven, Reporting System. *Int. J. Environ. Pollut.* **2012**, *48*, 262–272. [[CrossRef](#)]
22. Corradini, S.; Guerrieri, L.; Stelitano, D.; Salerno, G.; Scollo, S.; Merucci, L.; Prestifilippo, M.; Musacchio, M.; Silvestri, M.; Lombardo, V.; et al. Near Real-Time Monitoring of the Christmas 2018 Etna Eruption Using SEVIRI and Products Validation. *Remote Sens.* **2020**, *12*, 1336. [[CrossRef](#)]
23. Page, M.J.; McKenzie, J.E.; Bossuyt, P.M.; Boutron, I.; Hoffmann, T.C.; Mulrow, C.D.; Shamseer, L.; Tetzlaff, J.M.; Akl, E.A.; Brennan, S.E.; et al. The PRISMA 2020 Statement: An Updated Guideline for Reporting Systematic Reviews. *Rev. Panam. Salud Publica Pan Am. J. Public Health* **2022**, *46*, e112. [[CrossRef](#)]
24. Mupepi, O.; Marambanyika, T.; Matsa, M.M.; Dube, T. A Systematic Review on Remote Sensing of Wetland Environments. *Trans. R. Soc. S. Afr.* **2024**, 1–19. [[CrossRef](#)]
25. Höhl, A.; Obadic, I.; Torres, M.Á.F.; Najjar, H.; Oliveira, D.; Akata, Z.; Dengel, A.; Zhu, X.X. Opening the Black-Box: A Systematic Review on Explainable AI in Remote Sensing. *arXiv* **2024**, arXiv:2402.1379. [[CrossRef](#)]
26. Li, C.F.; Dai, Y.Y.; Zhao, J.J.; Yin, J.Y.; Xue, D.; Zhou, S.Q. Diffusion Source Detection of Volcanic Ash Cloud Using MODIS Satellite Data. *J. Indian Soc. Remote Sens.* **2014**, *42*, 611–619. [[CrossRef](#)]
27. Turner, W.; Rondinini, C.; Pettorelli, N.; Mora, B.; Leidner, A.K.; Szantoi, Z.; Buchanan, G.; Dech, S.; Dwyer, J.; Herold, M.; et al. Free and Open-Access Satellite Data Are Key to Biodiversity Conservation. *Biol. Conserv.* **2015**, *182*, 173–176. [[CrossRef](#)]
28. Bugliaro, L.; Piontek, D.; Kox, S.; Schmidl, M.; Mayer, B.; Müller, R.; Vázquez-Navarro, M.; Peters, D.M.; Grainger, R.G.; Gasteiger, J.; et al. VADUGS: A Neural Network for the Remote Sensing of Volcanic Ash with MSG/SEVIRI Trained with Synthetic Thermal Satellite Observations Simulated with a Radiative Transfer Model. *Nat. Hazards Earth Syst. Sci.* **2022**, *22*, 1029–1054. [[CrossRef](#)]
29. Prata, A.J. Infrared Radiative Transfer Calculations for Volcanic Ash Clouds. *Geophys. Res. Lett.* **1989**, *16*, 1293–1296. [[CrossRef](#)]
30. Yin, J.-Y.; Dong, J.-S.; Li, C.-F.; Zhao, J.-J. A New Detection Method of Volcanic Ash Cloud Based on MODIS Image. *J. Indian Soc. Remote Sens.* **2015**, *43*, 429–437. [[CrossRef](#)]
31. Marchese, F.; Ciampa, M.; Filizzola, C.; Lacava, T.; Mazzeo, G.; Pergola, N.; Tramutoli, V. On the Exportability of Robust Satellite Techniques (RST) for Active Volcano Monitoring. *Remote Sens.* **2010**, *2*, 1575–1588. [[CrossRef](#)]
32. Marchese, F.; Falconieri, A.; Pergola, N.; Tramutoli, V. Monitoring the Agung (Indonesia) Ash Plume of November 2017 by Means of Infrared Himawari 8 Data. *Remote Sens.* **2018**, *10*, 919. [[CrossRef](#)]
33. Prata, A.J. Observations Of Volcanic Ash Clouds In The 10-12-Mu-M Window Using Avhrr/2 Data. *Int. J. Remote Sens.* **1989**, *10*, 751–761. [[CrossRef](#)]
34. Hedelt, P.; Efremenko, D.S.; Loyola, D.G.; Spurr, R.; Clarisse, L. Sulfur Dioxide Layer Height Retrieval from Sentinel-5 Precursor/TROPOMI Using FP_ILM. *Atmos. Meas. Tech.* **2019**, *12*, 5503–5517. [[CrossRef](#)]

35. de Laat, A.; Vazquez-Navarro, M.; Theys, N.; Stammes, P. Analysis of Properties of the 19 February 2018 Volcanic Eruption of Mount Sinabung in S5P/TROPOMI and Himawari-8 Satellite Data. *Nat. Hazards Earth Syst. Sci.* **2020**, *20*, 1203–1217. [[CrossRef](#)]
36. Piscini, A.; Corradini, S.; Marchese, F.; Merucci, L.; Pergola, N.; Tramutoli, V. Volcanic Ash Cloud Detection from Space: A Comparison between the RST_{ASH} Technique and the Water Vapour Corrected BTM Procedure. *Geomat. Nat. Hazards Risk* **2011**, *2*, 263–277. [[CrossRef](#)]
37. Marchese, F.; Filizzola, C.; Mazzeo, G.; Pergola, N.; Sannazzaro, F.; Tramutoli, V. Assessment and Validation in Time Domain of a Robust Satellite Technique (RST_{ASH}) for Ash Cloud Detection. *Geomat. Nat. Hazards Risk* **2011**, *2*, 247–262. [[CrossRef](#)]
38. Thomas, H.E.; Prata, A.J. Sulphur Dioxide as a Volcanic Ash Proxy during the April-May 2010 Eruption of Eyjafjallajökull Volcano, Iceland. *Atmos. Chem. Phys.* **2011**, *11*, 6871–6880. [[CrossRef](#)]
39. Zhu, L.; Liu, J.; Liu, C.; Wang, M. Satellite Remote Sensing of Volcanic Ash Cloud in Complicated Meteorological Conditions. *Sci. China-Earth Sci. Sci. China Earth Sci.* **2011**, *54*, 1789–1795. [[CrossRef](#)]
40. Scollo, S.; Kahn, R.A.; Nelson, D.L.; Coltelli, M.; Diner, D.J.; Garay, M.J.; Realmuto, V.J. MISR Observations of Etna Volcanic Plumes. *J. Geophys. Res. Atmos.* **2012**, *117*, D06210. [[CrossRef](#)]
41. Kahn, R.A.; Limbacher, J. Eyjafjallajökull Volcano Plume Particle-Type Characterization from Space-Based Multi-Angle Imaging. *Atmos. Chem. Phys.* **2012**, *12*, 9459–9477. [[CrossRef](#)]
42. Christopher, S.A.; Feng, N.; Naeger, A.; Johnson, B.; Marenco, F. Satellite Remote Sensing Analysis of the 2010 Eyjafjallajökull Volcanic Ash Cloud over the North Sea during 4–18 May 2010. *J. Geophys. Res. Atmos.* **2012**, *117*, D00U20. [[CrossRef](#)]
43. Flemming, J.; Inness, A. Volcanic Sulfur Dioxide Plume Forecasts Based on UV Satellite Retrievals for the 2011 Grimsvotn and the 2010 Eyjafjallajökull Eruption. *J. Geophys. Res. Atmos.* **2013**, *118*, 10172–10189. [[CrossRef](#)]
44. Zaksek, K.; Hort, M.; Zaletelj, J.; Langmann, B. Monitoring Volcanic Ash Cloud Top Height through Simultaneous Retrieval of Optical Data from Polar Orbiting and Geostationary Satellites. *Atmos. Chem. Phys.* **2013**, *13*, 2589–2606. [[CrossRef](#)]
45. Ekstrand, A.L.; Webley, P.W.; Garay, M.J.; Dehn, J.; Prakash, A.; Nelson, D.L.; Dean, K.G.; Steensen, T. A Multi-Sensor Plume Height Analysis of the 2009 Redoubt Eruption. *J. Volcanol. Geotherm. Res.* **2013**, *259*, 170–184. [[CrossRef](#)]
46. Marchese, F.; Falconieri, A.; Pergola, N.; Tramutoli, V. A Retrospective Analysis of the Shinmoedake (Japan) Eruption of 26–27 January 2011 by Means of Japanese Geostationary Satellite Data. *J. Volcanol. Geotherm. Res.* **2014**, *269*, 1–13. [[CrossRef](#)]
47. Corradini, S.; Pugnaghi, S.; Piscini, A.; Guerrieri, L.; Merucci, L.; Picchiani, M.; Chini, M. Volcanic Ash and SO₂ Retrievals Using Synthetic MODIS TIR Data: Comparison between Inversion Procedures and Sensitivity Analysis. *Ann. Geophys.* **2014**, *57*. [[CrossRef](#)]
48. Cooke, M.C.; Francis, P.N.; Millington, S.; Saunders, R.; Witham, C. Detection of the Grimsvotn 2011 Volcanic Eruption Plumes Using Infrared Satellite Measurements. *Atmos. Sci. Lett.* **2014**, *15*, 321–327. [[CrossRef](#)]
49. Koukoulis, M.E.; Clarisse, L.; Carboni, E.; van Gent, J.; Spinetti, C.; Balis, D.; Dimopoulos, S.; Grainger, R.; Theys, N.; Tampellini, L.; et al. Intercomparison of Metop-A SO₂ Measurements during the 2010–2011 Icelandic Eruptions. *Ann. Geophys.* **2015**, *57*. [[CrossRef](#)]
50. Kylling, A.; Kahnert, M.; Lindqvist, H.; Nousiainen, T. Volcanic Ash Infrared Signature: Porous Non-Spherical Ash Particle Shapes Compared to Homogeneous Spherical Ash Particles. *Atmos. Meas. Tech.* **2014**, *7*, 919–929. [[CrossRef](#)]
51. Li, C.F.; Dai, Y.Y.; Zhao, J.J.; Zhou, S.Q.; Yin, J.Y.; Xue, D. Remote Sensing Monitoring of Volcanic Ash Clouds Based on PCA Method. *Acta Geophys.* **2015**, *63*, 432–450. [[CrossRef](#)]
52. Guerrieri, L.; Merucci, L.; Corradini, S.; Pugnaghi, S. Evolution of the 2011 Mt. Etna Ash and SO₂ Lava Fountain Episodes Using SEVIRI Data and VPR Retrieval Approach. *J. Volcanol. Geotherm. Res.* **2015**, *291*, 63–71. [[CrossRef](#)]
53. Kylling, A. Ash and Ice Clouds during the Mt Kelud February 2014 Eruption as Interpreted from IASI and AVHRR/3 Observations. *Atmos. Meas. Tech.* **2016**, *9*, 2103–2117. [[CrossRef](#)]
54. Merucci, L.; Zaksek, K.; Carboni, E.; Corradini, S. Stereoscopic Estimation of Volcanic Ash Cloud-Top Height from Two Geostationary Satellites. *Remote Sens.* **2016**, *8*, 206. [[CrossRef](#)]
55. Pugnaghi, S.; Guerrieri, L.; Corradini, S.; Merucci, L. Real Time Retrieval of Volcanic Cloud Particles and SO₂ by Satellite Using an Improved Simplified Approach. *Atmos. Meas. Tech.* **2016**, *9*, 3053–3062. [[CrossRef](#)]
56. Toyos, G.; Mingari, L.; Pujol, G.; Villarosa, G. Investigating the Nature of an Ash Cloud Event in Southern Chile Using Remote Sensing: Volcanic Eruption or Resuspension? *Remote Sens. Lett.* **2017**, *8*, 146–155. [[CrossRef](#)]
57. Zhu, L.; Li, J.; Zhao, Y.Y.; Gong, H.; Li, W.J. Retrieval of Volcanic Ash Height from Satellite-Based Infrared Measurements. *J. Geophys. Res. Atmos.* **2017**, *122*, 5364–5379. [[CrossRef](#)]
58. Biondi, R.; Steiner, A.K.; Kirchengast, G.; Brenot, H.; Rieckh, T. Supporting the Detection and Monitoring of Volcanic Clouds: A Promising New Application of Global Navigation Satellite System Radio Occultation. *Adv. Space Res.* **2017**, *60*, 2707–2722. [[CrossRef](#)]
59. Efremenko, D.S.; Loyola, D.G.; Hedelt, P.; Spurr, R.J.D. Volcanic SO₂ Plume Height Retrieval from UV Sensors Using a Full-Physics Inverse Learning Machine Algorithm. *Int. J. Remote Sens.* **2017**, *38*, 1–27. [[CrossRef](#)]
60. Carn, S.A.; Krotkov, N.A.; Fisher, B.L.; Li, C.; Prata, A.J. First Observations of Volcanic Eruption Clouds From the L1 Earth-Sun Lagrange Point by DSCOVR/EPIC. *Geophys. Res. Lett.* **2018**, *45*, 11456–11464. [[CrossRef](#)]
61. Marzano, F.S.; Corradini, S.; Mereu, L.; Kylling, A.; Montopoli, M.; Cimini, D.; Merucci, L.; Stelitano, D. Multisatellite Multisensor Observations of a Sub-Plinian Volcanic Eruption: The 2015 Calbuco Explosive Event in Chile. *IEEE Trans. Geosci. Remote Sens.* **2018**, *56*, 2597–2612. [[CrossRef](#)]

62. de Michele, M.; Raucoules, D.; Corradini, S.; Merucci, L.; Salerno, G.; Sellitto, P.; Carboni, E. Volcanic Cloud Top Height Estimation Using the Plume Elevation Model Procedure Applied to Orthorectified Landsat 8 Data. Test Case: 26 October 2013 Mt. Etna Eruption. *Remote Sens.* **2019**, *11*, 785. [[CrossRef](#)]
63. Carboni, E.; Mather, T.A.; Schmidt, A.; Grainger, R.G.; Pfeffer, M.A.; Ialongo, I.; Theys, N. Satellite-Derived Sulfur Dioxide (SO₂) Emissions from the 2014–2015 Holuhraun Eruption (Iceland). *Atmos. Chem. Phys.* **2019**, *19*, 4851–4862. [[CrossRef](#)]
64. Liu, L.; Sun, X.K. Volcanic Ash Cloud Diffusion From Remote Sensing Image Using LSTM-CA Method. *IEEE Access* **2020**, *8*, 54681–54690. [[CrossRef](#)]
65. Schneider, D.J.; Van Eaton, A.R.; Wallace, K.L. Satellite Observations of the 2016–2017 Eruption of Bogoslof Volcano: Aviation and Ash Fallout Hazard Implications from a Water-Rich Eruption. *Bull. Volcanol.* **2020**, *82*, 29. [[CrossRef](#)]
66. Pailot-Bonnétat, S.; Harris, A.J.L.; Calvari, S.; De Michele, M.; Gurioli, L. Plume Height Time-Series Retrieval Using Shadow in Single Spatial Resolution Satellite Images. *Remote Sens.* **2020**, *12*, 3951. [[CrossRef](#)]
67. Zhu, W.R.; Zhu, L.; Li, J.; Sun, H.F. Retrieving Volcanic Ash Top Height through Combined Polar Orbit Active and Geostationary Passive Remote Sensing Data. *Remote Sens.* **2020**, *12*, 953. [[CrossRef](#)]
68. Liu, L.; Li, C.F.; Sun, X.K.; Zhao, J.J. Monitoring of Volcanic Ash Cloud from Heterogeneous Data Using Feature Fusion and Convolutional Neural Networks-Long Short-Term Memory. *Neural Comput. Appl.* **2021**, *33*, 667–679. [[CrossRef](#)]
69. Corradini, S.; Guerrieri, L.; Brenot, H.; Clarisse, L.; Merucci, L.; Pardini, F.; Prata, A.J.; Realmuto, V.J.; Stelitano, D.; Theys, N. Tropospheric Volcanic SO₂ Mass and Flux Retrievals from Satellite. The Etna December 2018 Eruption. *Remote Sens.* **2021**, *13*, 2225. [[CrossRef](#)]
70. Filei, A.A.; Marengo, F. Retrieval of Volcanic Ash Parameters from Satellite Data. *Russ. Meteorol. Hydrol.* **2021**, *46*, 269–279. [[CrossRef](#)]
71. Guermazi, H.; Sellitto, P.; Cuesta, J.; Eremenko, M.; Lachatre, M.; Mailler, S.; Carboni, E.; Salerno, G.; Caltabiano, T.; Menut, L.; et al. Quantitative Retrieval of Volcanic Sulphate Aerosols from IASI Observations. *Remote Sens.* **2021**, *13*, 1808. [[CrossRef](#)]
72. Fedkin, N.M.; Li, C.; Krotkov, N.A.; Hedelt, P.; Loyola, D.G.; Dickerson, R.R.; Spurr, R. Volcanic SO₂ Effective Layer Height Retrieval for the Ozone Monitoring Instrument (OMI) Using a Machine-Learning Approach. *Atmos. Meas. Tech.* **2021**, *14*, 3673–3691. [[CrossRef](#)]
73. Gorkavyi, N.; Krotkov, N.; Li, C.; Lait, L.; Colarco, P.; Carn, S.; DeLand, M.; Newman, P.; Schoeberl, M.; Taha, G.; et al. Tracking Aerosols and SO₂ Clouds from the Raikoke Eruption: 3D View from Satellite Observations. *Atmos. Meas. Tech.* **2021**, *14*, 7545–7563. [[CrossRef](#)]
74. Koukouli, M.E.; Michailidis, K.; Hedelt, P.; Taylor, I.A.; Inness, A.; Clarisse, L.; Balis, D.; Efremenko, D.; Loyola, D.; Grainger, R.G.; et al. Volcanic SO₂ Layer Height by TROPOMI/S5P: Evaluation against IASI/MetOp and CALIOP/CALIPSO Observations. *Atmos. Chem. Phys.* **2022**, *22*, 5665–5683. [[CrossRef](#)]
75. Carr, J.L.; Horváth, A.; Wu, D.L.; Friberg, M.D. Stereo Plume Height and Motion Retrievals for the Record-Setting Hunga Tonga-Hunga Ha’apai Eruption of 15 January 2022. *Geophys. Res. Lett.* **2022**, *49*, e2022GL098131. [[CrossRef](#)]
76. Piontek, D.; Bugliaro, L.; Kar, J.; Schumann, U.; Marengo, F.; Plu, M.; Voigt, C. The New Volcanic Ash Satellite Retrieval VACOS Using MSG/SEVIRI and Artificial Neural Networks: 2. Validation. *Remote Sens.* **2021**, *13*, 3128. [[CrossRef](#)]
77. Petracca, I.; De Santis, D.; Picchiani, M.; Corradini, S.; Guerrieri, L.; Prata, F.; Merucci, L.; Stelitano, D.; Del Frate, F.; Salvucci, G.; et al. Volcanic Cloud Detection Using Sentinel-3 Satellite Data by Means of Neural Networks: The Raikoke 2019 Eruption Test Case. *Atmos. Meas. Tech.* **2022**, *15*, 7195–7210. [[CrossRef](#)]
78. Taha, G.; Loughman, R.; Colarco, P.R.; Zhu, T.; Thomason, L.W.; Jaross, G.; Taha, G.; Loughman, R.; Colarco, P.R.; Zhu, T.; et al. Tracking the 2022 Hunga Tonga-Hunga Ha’apai Aerosol Cloud in the Upper and Middle Stratosphere Using Space-Based Observations. *Geophys. Res. Lett.* **2022**, *49*, e2022GL100091. [[CrossRef](#)] [[PubMed](#)]
79. Torrisi, F.; Amato, E.; Corradino, C.; Mangiagli, S.; Del Negro, C. Characterization of Volcanic Cloud Components Using Machine Learning Techniques and SEVIRI Infrared Images. *Sensors* **2022**, *22*, 7712. [[CrossRef](#)] [[PubMed](#)]
80. Wen, S.M.; Rose, W.I. Retrieval of Sizes and Total Masses of Particles in Volcanic Clouds Using AVHRR Bands 4 and 5. *J. Geophys. Res. Atmos.* **1994**, *99*, 5421–5431. [[CrossRef](#)]
81. Prata, A.J.; Grant, I.F. Retrieval of Microphysical and Morphological Properties of Volcanic Ash Plumes from Satellite Data: Application to Mt Ruapehu, New Zealand. *Q. J. R. Meteorol. Soc.* **2001**, *127*, 2153–2179. [[CrossRef](#)]
82. Scollo, S.; Boselli, A.; Coltelli, M.; Leto, G.; Pisani, G.; Spinelli, N.; Wang, X. Monitoring Etna Volcanic Plumes Using a Scanning LiDAR. *Bull. Volcanol.* **2012**, *74*, 2383–2395. [[CrossRef](#)]
83. Pisani, G.; Boselli, A.; Coltelli, M.; Leto, G.; Pica, G.; Scollo, S.; Spinelli, N.; Wang, X. Lidar Depolarization Measurement of Fresh Volcanic Ash from Mt. Etna, Italy. *Atmos. Environ.* **2012**, *62*, 34–40. [[CrossRef](#)]
84. Marzano, F.S.; Lamantea, M.; Montopoli, M.; Herzog, M.; Graf, H.; Cimini, D. Microwave Remote Sensing of the 2011 Plinian Eruption of the Grimsvotn Icelandic Volcano. *Remote Sens. Environ.* **2013**, *129*, 168–184. [[CrossRef](#)]
85. Schneider, D.J.; Hoblitt, R.P. Doppler Weather Radar Observations of the 2009 Eruption of Redoubt Volcano, Alaska. *J. Volcanol. Geotherm. Res.* **2013**, *259*, 133–144. [[CrossRef](#)]
86. Burton, M.R.; Salerno, G.G.; D’Auria, L.; Caltabiano, T.; Murè, F.; Maugeri, R. SO₂ Flux Monitoring at Stromboli with the New Permanent INGV SO₂ Camera System: A Comparison with the FLAME Network and Seismological Data. *J. Volcanol. Geotherm. Res.* **2015**, *300*, 95–102. [[CrossRef](#)]

87. Lopez, T.; Thomas, H.E.; Prata, A.J.; Amigo, A.; Fee, D.; Moriano, D. Volcanic Plume Characteristics Determined Using an Infrared Imaging Camera. *J. Volcanol. Geotherm. Res.* **2015**, *300*, 148–166. [[CrossRef](#)]
88. Scollo, S.; Boselli, A.; Coltelli, M.; Leto, G.; Pisani, G.; Prestifilippo, M.; Spinelli, N.; Wang, X. Volcanic Ash Concentration during the 12 August 2011 Etna Eruption. *Geophys. Res. Lett.* **2015**, *42*, 2634–2641. [[CrossRef](#)]
89. Vidal, L.; Nesbitt, S.W.; Salio, P.; Farias, C.; Nicora, M.G.; Osores, M.S.; Mereu, L.; Marzano, F.S. C-Band Dual-Polarization Radar Observations of a Massive Volcanic Eruption in South America. *IEEE J. Sel. Top. Appl. Earth Obs. Remote Sens.* **2017**, *10*, 960–974. [[CrossRef](#)]
90. Pfeffer, M.A.; Bergsson, B.; Barsotti, S.; Stefánsdóttir, G.; Galle, B.; Arellano, S.; Conde, V.; Donovan, A.; Ilyinskaya, E.; Burton, M.; et al. Ground-Based Measurements of the 2014–2015 Holuhraun Volcanic Cloud (Iceland). *Geosciences* **2018**, *8*, 29. [[CrossRef](#)]
91. Sellitto, P.; Spampinato, L.; Salerno, G.G.; La Spina, A. Aerosol Optical Properties of Pacaya Volcano Plume Measured with a Portable Sun-Photometer. *Geosciences* **2018**, *8*, 36. [[CrossRef](#)]
92. Mereu, L.; Scollo, S.; Mori, S.; Boselli, A.; Leto, G.; Marzano, F.S. Maximum-Likelihood Retrieval of Volcanic Ash Concentration and Particle Size From Ground-Based Scanning Lidar. *IEEE Trans. Geosci. Remote Sens.* **2018**, *56*, 5824–5842. [[CrossRef](#)]
93. Freret-Lorgeril, V.; Donnadiou, F.; Scollo, S.; Provost, A.; Fréville, P.; Guéhenneux, Y.; Hervier, C.; Prestifilippo, M.; Coltelli, M. Mass Eruption Rates of Tephra Plumes During the 2011–2015 Lava Fountain Paroxysms at Mt. Etna From Doppler Radar Retrievals. *Front. Earth Sci.* **2018**, *6*, 73. [[CrossRef](#)]
94. Wood, K.; Thomas, H.; Watson, M.; Calway, A.; Richardson, T.; Stebel, K.; Naismith, A.; Berthoud, L.; Lucas, J. Measurement of Three Dimensional Volcanic Plume Properties Using Multiple Ground Based Infrared Cameras. *Isprs J. Remote Sens.* **2019**, *154*, 163–175. [[CrossRef](#)]
95. Poffo, D.A.; Caranti, G.M.; Comes, R.A.; Rodriguez, A. A New Ash Concentration Estimation Method Using Polarimetric Data: The RMA Observation of the 2015 Calbuco Eruption. *Remote Sens. Appl. Soc. Environ.* **2019**, *13*, 224–233. [[CrossRef](#)]
96. Huret, N.; Segonne, C.; Payan, S.; Salerno, G.; Catoire, V.; Ferrec, Y.; Roberts, T.; Fossi, A.P.; Rodriguez, D.; Croizé, L.; et al. Infrared Hyperspectral and Ultraviolet Remote Measurements of Volcanic Gas Plume at MT Etna during IMAGETNA Campaign. *Remote Sens.* **2019**, *11*, 1175. [[CrossRef](#)]
97. Marzano, F.S.; Mereu, L.; Scollo, S.; Donnadiou, F.; Bonadonna, C. Tephra Mass Eruption Rate From Ground-Based X-Band and L-Band Microwave Radars During the November 23, 2013, Etna Paroxysm. *IEEE Trans. Geosci. Remote Sens.* **2020**, *58*, 3314–3327. [[CrossRef](#)]
98. Ilanko, T.; Pering, T.D.; Wilkes, T.C.; Woitischek, J.; D’Aleo, R.; Aiuppa, A.; McGonigle, A.J.S.; Edmonds, M.; Garaebiti, E. Ultraviolet Camera Measurements of Passive and Explosive (Strombolian) Sulphur Dioxide Emissions at Yasur Volcano, Vanuatu. *Remote Sens.* **2020**, *12*, 2703. [[CrossRef](#)]
99. Fuchs, C.; Kuhn, J.; Bobrowski, N.; Platt, U. Quantitative Imaging of Volcanic SO₂ Plumes Using Fabry-Perot Interferometer Correlation Spectroscopy. *Atmos. Meas. Tech.* **2021**, *14*, 295–307. [[CrossRef](#)]
100. Mereu, L.; Scollo, S.; Boselli, A.; Leto, G.; Sanchez, R.Z.; Bonadonna, C.; Marzano, F.S. Dual-Wavelength Polarimetric Lidar Observations of the Volcanic Ash Cloud Produced during the 2016 Etna Eruption. *Remote Sens.* **2021**, *13*, 1728. [[CrossRef](#)]
101. Sicard, M.; Córdoba-Jabonero, C.; Barreto, A.; Welton, E.J.; Gil-Díaz, C.; Carvajal-Perez, C.V.; Comerón, A.; García, O.; García, R.; López-Cayuela, M.A.; et al. Volcanic Eruption of Cumbre Vieja, La Palma, Spain: A First Insight to the Particulate Matter Injected in the Troposphere. *Remote Sens.* **2022**, *14*, 2470. [[CrossRef](#)]
102. Bedoya-Velásquez, A.E.; Hoyos-Restrepo, M.; Barreto, A.; García, R.D.; Romero-Campos, P.M.; García, O.; Ramos, R.; Roininen, R.; Toledano, C.; Sicard, M.; et al. Estimation of the Mass Concentration of Volcanic Ash Using Ceilometers: Study of Fresh and Transported Plumes from La Palma Volcano. *Remote Sens.* **2022**, *14*, 5680. [[CrossRef](#)]
103. Mori, T.; Hashimoto, T.; Terada, A.; Yoshimoto, M.; Kazahaya, R.; Shinohara, H.; Tanaka, R. Volcanic Plume Measurements Using a UAV for the 2014 Mt. Ontake Eruption. *Earth Planets Space* **2016**, *68*, 49. [[CrossRef](#)]
104. Schellenberg, B.; Richardson, T.; Watson, M.; Greatwood, C.; Clarke, R.; Thomas, R.; Wood, K.; Freer, J.; Thomas, H.; Liu, E.; et al. Remote Sensing and Identification of Volcanic Plumes Using Fixed-Wing UAVs over Volcan de Fuego, Guatemala. *J. Field Robot.* **2019**, *36*, 1192–1211. [[CrossRef](#)]
105. Brosch, E. Volcanic Ash and Small Uncrewed Aerial Vehicle (SUAV) Interaction: In-Situ Observations and Laboratory Experiments on Aircraft Failure. *Front. Earth Sci.* **2022**, *10*, 810962. [[CrossRef](#)]
106. Spinei, E.; Carn, S.A.; Krotkov, N.A.; Mount, G.H.; Yang, K.; Krueger, A. Validation of Ozone Monitoring Instrument SO₂ Measurements in the Okmok Volcanic Cloud over Pullman, WA, July 2008. *J. Geophys. Res. Atmos.* **2010**, *115*, D00L08. [[CrossRef](#)]
107. Merucci, L.; Burton, M.; Corradini, S.; Salerno, G.G. Reconstruction of SO₂ Flux Emission Chronology from Space-Based Measurements. *J. Volcanol. Geotherm. Res.* **2011**, *206*, 80–87. [[CrossRef](#)]
108. Spinetti, C.; Salerno, G.G.; Caltabiano, T.; Carboni, E.; Clarisse, L.; Corradini, S.; Grainger, R.G.; Hedelt, P.A.; Koukouli, M.E.; Merucci, L.; et al. Volcanic SO₂ by UV-TIR Satellite Retrievals: Validation by Using Ground-Based Network at Mt. Etna. *Ann. Geophys.* **2015**, *57*. [[CrossRef](#)]
109. Ialongo, I.; Hakkarainen, J.; Kivi, R.; Anttila, P.; Krotkov, N.A.; Yang, K.; Li, C.; Tukiainen, S.; Hassinen, S.; Tamminen, J. Comparison of Operational Satellite SO₂ Products with Ground-Based Observations in Northern Finland during the Icelandic Holuhraun Fissure Eruption. *Atmos. Meas. Tech.* **2015**, *8*, 2279–2289. [[CrossRef](#)]

110. Corradini, S.; Montopoli, M.; Guerrieri, L.; Ricci, M.; Scollo, S.; Merucci, L.; Marzano, F.S.; Pugnaghi, S.; Prestifilippo, M.; Ventress, L.J.; et al. A Multi-Sensor Approach for Volcanic Ash Cloud Retrieval and Eruption Characterization: The 23 November 2013 Etna Lava Fountain. *Remote Sens.* **2016**, *8*, 58. [[CrossRef](#)]
111. Scollo, S.; Prestifilippo, M.; Bonadonna, C.; Cioni, R.; Corradini, S.; Degruyter, W.; Rossi, E.; Silvestri, M.; Biale, E.; Carparelli, G.; et al. Near-Real-Time Tephra Fallout Assessment at Mt. Etna, Italy. *Remote Sens.* **2019**, *11*, 2987. [[CrossRef](#)]
112. Freret-Lorgeril, V.; Bonadonna, C.; Corradini, S.; Donnadieu, F.; Guerrieri, L.; Lacanna, G.; Marzano, F.S.; Mereu, L.; Merucci, L.; Ripepe, M.; et al. Examples of Multi-Sensor Determination of Eruptive Source Parameters of Explosive Events at Mount Etna. *Remote Sens.* **2021**, *13*, 2097. [[CrossRef](#)]
113. Scollo, S.; Folch, A.; Coltelli, M.; Realmuto, V.J. Three-Dimensional Volcanic Aerosol Dispersal: A Comparison between Multiangle Imaging Spectroradiometer (MISR) Data and Numerical Simulations. *J. Geophys. Res. Atmos.* **2010**, *115*, D24210. [[CrossRef](#)]
114. Corradini, S.; Merucci, L.; Folch, A. Volcanic Ash Cloud Properties: Comparison Between MODIS Satellite Retrievals and FALL3D Transport Model. *IEEE Geosci. Remote Sens. Lett.* **2011**, *8*, 248–252. [[CrossRef](#)]
115. Matthias, V.; Auling, A.; Bieser, J.; Cuesta, J.; Geyer, B.; Langmann, B.; Serikov, I.; Mattis, I.; Minikin, A.; Mona, L.; et al. The Ash Dispersion over Europe during the Eyjafjallajökull Eruption—Comparison of CMAQ Simulations to Remote Sensing and Air-Borne in-Situ Observations. *Atmos. Environ.* **2012**, *48*, 184–194. [[CrossRef](#)]
116. Montopoli, M.; Cimini, D.; Lamantea, M.; Herzog, M.; Graf, H.F.; Marzano, F.S. Microwave Radiometric Remote Sensing of Volcanic Ash Clouds From Space: Model and Data Analysis. *IEEE Trans. Geosci. Remote Sens.* **2013**, *51*, 4678–4691. [[CrossRef](#)]
117. Dacre, H.F.; Grant, A.L.M.; Johnson, B.T. Aircraft Observations and Model Simulations of Concentration and Particle Size Distribution in the Eyjafjallajökull Volcanic Ash Cloud. *Atmos. Chem. Phys.* **2013**, *13*, 1277–1291. [[CrossRef](#)]
118. Boichu, M.; Menut, L.; Khvorostyanov, D.; Clarisse, L.; Clerbaux, C.; Turquety, S.; Coheur, P.F. Inverting for Volcanic SO₂ Flux at High Temporal Resolution Using Spaceborne Plume Imagery and Chemistry-Transport Modelling: The 2010 Eyjafjallajökull Eruption Case Study. *Atmos. Chem. Phys.* **2013**, *13*, 8569–8584. [[CrossRef](#)]
119. Osore, M.S.; Folch, A.; Collini, E.; Villarosa, G.; Durant, A.; Pujol, G.; Viramonte, J.G. Validation of the FALL3D Model for the 2008 Chaiten Eruption Using Field and Satellite Data. *Andean Geol.* **2013**, *40*, 262–276. [[CrossRef](#)]
120. Spinetti, C.; Barsotti, S.; Neri, A.; Buongiorno, M.F.; Doumaz, F.; Nannipieri, L. Investigation of the Complex Dynamics and Structure of the 2010 Eyjafjallajökull Volcanic Ash Cloud Using Multispectral Images and Numerical Simulations. *J. Geophys. Res. Atmos.* **2013**, *118*, 4729–4747. [[CrossRef](#)]
121. Moxnes, E.D.; Kristiansen, N.I.; Stohl, A.; Clarisse, L.; Durant, A.; Weber, K.; Vogel, A. Separation of Ash and Sulfur Dioxide during the 2011 Grimsvotn Eruption. *J. Geophys. Res. Atmos.* **2014**, *119*, 7477–7501. [[CrossRef](#)]
122. Kristiansen, N.I.; Prata, A.J.; Stohl, A.; Carn, S.A. Stratospheric Volcanic Ash Emissions From the 13 February 2014 Kelut Eruption. *Geophys. Res. Lett.* **2015**, *42*, 588–596. [[CrossRef](#)]
123. Liu, J.; Salmond, J.A.; Dirks, K.N.; Lindsay, J.M. Validation of Ash Cloud Modelling with Satellite Retrievals: A Case Study of the 16–17 June 1996 Mount Ruapehu Eruption. *Nat. Hazards* **2015**, *78*, 973–993. [[CrossRef](#)]
124. Crawford, A.M.; Stunder, B.J.B.; Ngan, F.; Pavolonis, M.J. Initializing HYSPLIT with Satellite Observations of Volcanic Ash: A Case Study of the 2008 Kasatochi Eruption. *J. Geophys. Res. Atmos.* **2016**, *121*, 10786–10803. [[CrossRef](#)]
125. Dare, R.A.; Smith, D.H.; Naughton, M.J. Ensemble Prediction of the Dispersion of Volcanic Ash from the 13 February 2014 Eruption of Kelut, Indonesia. *J. Appl. Meteorol. Clim.* **2016**, *55*, 61–78. [[CrossRef](#)]
126. Wilkins, K.L.; Western, L.M.; Watson, I.M. Simulating Atmospheric Transport of the 2011 Grimsvotn Ash Cloud Using a Data Insertion Update Scheme. *Atmos. Environ.* **2016**, *141*, 48–59. [[CrossRef](#)]
127. Tanaka, H.L.; Nakamichi, H.; Iguchi, M. PUFF Model Prediction of Volcanic Ash Plume Dispersal for Sakurajima Using MP Radar Observation. *Atmosphere* **2020**, *11*, 1240. [[CrossRef](#)]
128. Chai, T.F.; Crawford, A.; Stunder, B.; Pavolonis, M.J.; Draxler, R.; Stein, A. Improving Volcanic Ash Predictions with the HYSPLIT Dispersion Model by Assimilating MODIS Satellite Retrievals. *Atmos. Chem. Phys.* **2017**, *17*, 2865–2879. [[CrossRef](#)]
129. Sorokin, A.A.; Girina, O.A.; Lupyan, E.A.; Mal'kovskii, S.I.; Balashov, I.V.; Efremov, V.Y.; Kramareva, L.S.; Korolev, S.P.; Romanova, I.M.; Simonenko, E. V Satellite Observations and Numerical Simulation Results for the Comprehensive Analysis of Ash Cloud Transport during the Explosive Eruptions of Kamchatka Volcanoes. *Russ. Meteorol. Hydrol.* **2017**, *42*, 759–765. [[CrossRef](#)]
130. Poret, M.; Corradini, S.; Merucci, L.; Costa, A.; Andronico, D.; Montopoli, M.; Vulpiani, G.; Freret-Lorgeril, V. Reconstructing Volcanic Plume Evolution Integrating Satellite and Ground-Based Data: Application to the 23 November 2013 Etna Eruption. *Atmos. Chem. Phys.* **2018**, *18*, 4695–4714. [[CrossRef](#)]
131. Wu, X.; Griessbach, S.; Hoffmann, L. Long-Range Transport of Volcanic Aerosol from the 2010 Merapi Tropical Eruption to Antarctica. *Atmos. Chem. Phys.* **2018**, *18*, 15859–15877. [[CrossRef](#)]
132. Poret, M.; Costa, A.; Andronico, D.; Scollo, S.; Gouhier, M.; Cristaldi, A. Modeling Eruption Source Parameters by Integrating Field, Ground-Based, and Satellite-Based Measurements: The Case of the 23 February 2013 Etna Paroxysm. *J. Geophys. Res. Solid Earth* **2018**, *123*, 5427–5450. [[CrossRef](#)]
133. Pardini, F.; Queisser, M.; Naismith, A.; Watson, I.M.; Clarisse, L.; Burton, M.R. Initial Constraints on Triggering Mechanisms of the Eruption of Fuego Volcano (Guatemala) from 3 June 2018 Using IASI Satellite Data. *J. Volcanol. Geotherm. Res.* **2019**, *376*, 54–61. [[CrossRef](#)]
134. Clarisse, L.; Hurtmans, D.; Clerbaux, C.; Hadji-Lazaro, J.; Ngadi, Y.; Coheur, P.F. Retrieval of Sulphur Dioxide from the Infrared Atmospheric Sounding Interferometer (IASI). *Atmos. Meas. Tech.* **2012**, *5*, 581–594. [[CrossRef](#)]

135. Williams, D.B.; Ramsey, M.S.; Wickens, D.J.; Karimi, B. Identifying Eruptive Sources of Drifting Volcanic Ash Clouds Using Back-Trajectory Modeling of Spaceborne Thermal Infrared Data. *Bull. Volcanol.* **2019**, *81*, 53. [[CrossRef](#)]
136. Pardini, F.; Corradini, S.; Costa, A.; Ongaro, T.E.; Merucci, L.; Neri, A.; Stelitano, D.; Vitturi, M.D. Ensemble-Based Data Assimilation of Volcanic Ash Clouds from Satellite Observations: Application to the 24 December 2018 Mt. Etna Explosive Eruption. *Atmosphere* **2020**, *11*, 359. [[CrossRef](#)]
137. Paez, P.A.; Cogliati, M.G.; Caselli, A.T.; Monasterio, A.M. An Analysis of Volcanic SO₂ and Ash Emissions from Copahue Volcano. *J. S. Am. Earth Sci.* **2021**, *110*, 103365. [[CrossRef](#)]
138. Gunda, G.K.T.; Champatiray, P.K.; Chauhan, M.; Chauhan, P.; Ansary, M.; Singh, A.; Ketholia, Y.; Balaji, S. Modelling of Volcanic Ash with HYSPLIT and Satellite Observations: A Case Study of the 2018 Barren Island Volcano Eruption Event, Andaman Territory, India. *Curr. Sci.* **2021**, *121*, 529–538. [[CrossRef](#)]
139. Rizza, U.; Donnadieu, F.; Magazu, S.; Passerini, G.; Castorina, G.; Semprebello, A.; Morichetti, M.; Virgili, S.; Mancinelli, E. Effects of Variable Eruption Source Parameters on Volcanic Plume Transport: Example of the 23 November 2013 Paroxysm of Etna. *Remote Sens.* **2021**, *13*, 4037. [[CrossRef](#)]
140. Amiridis, V.; Kampouri, A.; Gkikas, A.; Misios, S.; Gialitaki, A.; Marinou, E.; Rennie, M.; Benedetti, A.; Solomos, S.; Zanis, P.; et al. Aeolus winds impact on volcanic ash early warning systems for aviation. *Sci. Rep.* **2023**, *13*, 7531. [[CrossRef](#)]
141. Mastin, L.G.; Van Eaton, A.R. Comparing Simulations of Umbrella-Cloud Growth and Ash Transport with Observations from Pinatubo, Kelud, and Calbuco Volcanoes. *Atmosphere* **2020**, *11*, 1038. [[CrossRef](#)]
142. Poulidis, A.P.; Phillips, J.C.; Renfrew, I.A.; Barclay, J.; Hogg, A.; Jenkins, S.F.; Robertson, R.; Pyle, D.M. Meteorological Controls on Local and Regional Volcanic Ash Dispersal. *Sci. Rep.* **2018**, *8*, 6873. [[CrossRef](#)]

Disclaimer/Publisher’s Note: The statements, opinions and data contained in all publications are solely those of the individual author(s) and contributor(s) and not of MDPI and/or the editor(s). MDPI and/or the editor(s) disclaim responsibility for any injury to people or property resulting from any ideas, methods, instructions or products referred to in the content.